Spring 2019

Unmanned aerial and traversing vehicle -- A mobile platform for bridge inspections

Clayton A. Fritsche

Department:

UNMANNED AERIAL AND TRAVERSING VEHICLE

-A MOBILE PLATFORM FOR BRIDGE INSPECTIONS

by

CLAYTON ANDREW FRITSCHE

A THESIS

Presented to the Faculty of the Graduate School of the

MISSOURI UNIVERSITY OF SCIENCE AND TECHNOLOGY

In Partial Fulfillment of the Requirements for the Degree

MASTER OF SCIENCE IN CIVIL ENGINEERING

2019

Approved by

Dr. Genda Chen, Advisor
Dr. K. Krishnamurthy
Dr. Guirong Yan

ABSTRACT

Unmanned aerial vehicles (UAVs), also known as drones, have been rapidly growing in popularity since their creation. This study aimed to create a robotic platform used to assist in the inspection process of the nation's aging and deteriorating bridges. To this end, a multimodal inspection robot that utilized both flying and driving technologies, was designed, analyzed, and tested for aerial, traversing, and their transitional operability. The design, herein referred to as the "BridgeBot", was evaluated both computationally and experimentally. A finite element model of the BridgeBot was established and analyzed under static loading scenarios to help determine stress distributions and locate areas of concern. The prototype BridgeBot was then tested in the laboratory to evaluate the drone structure and ability to perform to its design intent. During a bridge inspection, the BridgeBot would deploy as a multirotor UAV and fly to the underside of a bridge girder. It would then utilize its specifically designed clamping system with custom rollers to engage and traverse along the girder flange. This transition from flying to traversing mode may not only significantly save battery, making it feasible for the BridgeBot to operate for longer periods of time, but also provide a stable platform for various cameras and nondestructive evaluation devices to acquire quality data. Although the design focused on steel girder bridges, it may later be adjusted for concrete girder bridges. Initial test results indicated the feasibility of the BridgeBot to transition from flying to traversing mode. However, upon landing, some of the electrical wires secured to the bottom of the flexible rotor arms were detached due to significant arm deformations causing the propellers to dislodge the wire connection under impact loading.

ACKNOWLEDGMENTS

In the pursuance of this master's degree, I have received incredible support. Dr. Genda Chen, who has been my advisor throughout my undergraduate and graduate degree and who has guided me though this challenging yet extremely rewarding process, placed his faith in me to complete this project and has made me forever grateful.

Without the help of the MinerFly research team at Missouri S&T, this project would have never been possible. Their expertise in the field of aerial robotics has been irreplaceable. System Administrator, Alec Reven, and Undergraduate Assistants, Steven Grassman, Andrew Gerth, Ben Ross, and Peter Pogorzelski allowed for the design, modeling, and fabrication to be completed entirely by Missouri S&T students and faculty.

I would like to acknowledge other members of the campus faculty and staff who have also assisted with the project. My advisory committee, Dr. Guirong Yan and Dr. K. Krishnamurthy, are to thank for the review and approval of this thesis and the evaluation of my final defense. Departmental staff including Gary Abbott, Brian Swift, and Greg Leckrone were crucial to the formation and implementation of laboratory experimentation. Dr. Joel Burken has also provided valuable insight throughout my education towards the completion of this degree for which I sincerely appreciate.

Though many people have helped to complete this research, my utmost gratitude is reserved for my family. Their emotional support and unwavering confidence in me have given me the ability to persevere the long nights and stressful examinations that brought me to this point. To my parents, Les and Kim, my brother, Garrett, and my fiancé, Taylor, thank you.

TABLE OF CONTENTS

Page

LIST OF ILLUSTRATIONS

Page

LIST OF TABLES

Page

ABBREVIATIONS

Symbol	Description
AASHTO	American Association of State Highway and Transportation Officials
ASCE	American Society of Civil Engineers
ASTM	American Society for Testing and Materials
BIRM	Bridge Inspector's Reference Manual
DOT	Department of Transportation
FAA	Federal Aviation Administration
FEA	Finite Element Analysis
FHWA	Federal Highway Administration
GPS	Global Positioning System
NBI	National Bridge Inventory
NBIS	National Bridge Inspection Standards
UAV	Unmanned Aerial Vehicle

NOMENCLATURE

Symbol	Description
A	Average cross-sectional area, mm^2 (in^2)
B_y	Percent Bending, %
CV	Sample Coefficient of Variation, %
E^{chord}	Tensile Chord Modulus of Elasticity, GPa (psi)
F^{cu}	Ultimate Compressive Strength, MPa (psi)
F^{tu}	Ultimate Tensile Strength, MPa (psi)
G^{chord}	Shear Chord Modulus of Elasticity, MPa (psi)
n	Number of Specimens
P_i	Force at *i*th Data Point, N (lbf)
P^{max}	Maximum force before failure, N (lbf)
S_{n-1}	Sample Standard Deviation
x	Sample Mean (Average)
x_i	Measured or Derived Property
γ_i	Engineering Shear Strain at *i*th Data Point, με
$\Delta\gamma$	Difference Between Two Engineering Shear Strain Points, ε
$\Delta\tau$	Difference in Applied Shear Stress Between Two Points, MPa (psi)
$\varepsilon_{+45°}$	+45° Normal Strain at *i*th Data Point, με
$\varepsilon_{-45°}$	-45° Normal Strain at *i*th Data Point, με
ε_b	Indicated Strain From Back Transducer, με
ε_f	Indicated Strain From Front Transducer, με

ε_l	Longitudinal Strain, με
ε_t	Transverse Strain, με
ν	Poisson's Ratio
σ_l	Longitudinal Stress, MPa (psi)
τ_i	Shear Stress at *i*th Data Point, MPa (psi)

1. INTRODUCTION

1.1. MOTIVATION OF STUDY

According to the American Society of Civil Engineer's (ASCE) 2017 Infrastructure Report Card, the United States contains 614,387 bridges, 9.1% (56,007) of which are listed as being structurally deficient [1]. As of 2016, these structurally deficient bridges were supporting on average 188 million vehicles per day [1]. 39% (239,611) of the total bridges are also 50 years old or older, despite their typical 50-year design life [1]. Whether there is a stream or river, canyon or valley, or just a rugged patch of earthly terrain, there is likely a bridge to cross it, and there will continue to be so for the foreseeable future.

Prior to 1968, safety inspections and maintenance of bridges was of little concern. Bridges could go years being structurally ignored, well past their design life. This all changed in December of 1967 when the Silver Bridge at Point Pleasant, West Virginia, came crashing down into the Ohio River, killing 46 people [2]. This destruction quickly set in motion the enactment of an additional section to the Federal Highway Act of 1968, requiring the establishment of a national bridge inspection standard by the Secretary of Transportation. This included the development of a program to train bridge inspectors [2]. In 1971, the *National Bridge Inspection Standards* (NBIS) established a national policy for inspection procedures, frequency, personnel qualifications, inspection reports, and also called for the maintenance of the state bridge inventory [2]. Three manuals were developed to supplement the NBIS including the Federal Highway Administration's (FHWA) *Bridge Inspector's Training Manual 70*, The American Association of State Highway Officials' (AASHO), who shortly after changed their name to American Association of State

Highway and Transportation Officials (AASHTO), *Manual for Maintenance Inspection of Bridges*, and the FHWA *Recording and Coding Guide for the Structure Inventory and Appraisal of the Nation's Bridges* (Coding Guide) [2]. Revisions, code replacements, and manual additions have since been created to keep up with the growing concern for proper and concise inspection practices and bridge management. These changes have occurred for a variety of reasons. A few of these reasons, including a 1988 technical advisor, *Scour at Bridges*, was the response to a structural failure or collapse [2]. This particular case being the collapse of New York's Schoharie Creek Bridge in 1987. Even with all these references in place, there is a constant need for improved methods as long as new bridges are created with changing design methods, failures occur in unforeseen locations, and infrastructure continues to age. The most current collective source of bridge inspection practices is the *Bridge Inspector's Reference Manual* (BIRM) which was updated in 2012 [2]. The BIRM includes items pertaining to safety, bridge terminology, reporting procedures, inspection and evaluation of specific bridge types, a copy of the most recent NBIS, and more. Though they are no longer legally required, bridge management systems are also in place to assist with keeping records of bridges. Currently, the most common bridge management system, used in 39 states, is AASHTOWare, formerly known as Pontis, created by AASHTO [3]. These systems allow owners to maximize their investment by determining which bridges are in the most need of repair based on public safety and budgetary restrictions.

Routine inspections are a necessary process in order to reduce risk and maintain the structural integrity of bridges. These inspections allow for structural concerns to be determined and analyzed prior to causing a safety issue. They are designed to prevent bridge failure and protect the safety of the citizens who used them. Without consistent

monitoring and documentation of the bridge deck, superstructure, and substructure, the risk of failure is uncontrolled. Routine inspections are mandated to be performed every two years as required by the NBIS [4]. These inspections are performed from the deck, ground, or water beneath the bridge, depending on the bridge design and location. Comprehensive fracture critical inspections are also performed when recommend by the inspector after routine inspection. These inspections require a close eye visual inspection (<24") which may include the use of dyes, magnetic particles, or ultrasonic techniques [4]. The time it takes per inspection varies greatly depending on how in depth the inspection is, the size of bridge, weather conditions, etc.

The most common bridge inspection method involves the use of aerial work platforms (AWP). This includes snooper trucks and boom lifts shown in Figure 1.1, along with other under bridge inspection vehicles that allow the inspector to examine each element of the bridge's structural system. Each of these AWP provide specific benefits which allow them to be more economical in different situations. Snooper trucks provide access to the underside of the structure over the side of the bridge. This is particularly useful on narrow bridges in which the articulated arm can provide the reach necessary to extend to the center of the bridge. Situations where the area beneath the superstructure of the bridge is inaccessible also encourages the use of snooper trucks. When spans are wide and the bridge underclearance allows for it, boom lifts, or boom trucks, may be used to perform the inspection. The lifts on these vehicles can provide access from the ground surface, while also having the option to be secured to barges for bridge inspections over waterways.

Figure 1.1. Common Aerial Work Platforms:
Snooper Truck (left) [5], Boom Lift Secured to Barge (right) [6]

Rope access is another method of bridge inspection (Figure 1.2). This method involves certified rope access professionals using climbing equipment to repel below the bridge. It is typically used when snooper trucks and boom lifts are not able to approach the bridge superstructure. Using rope is also a common technique for large, above deck supported bridge types including over truss, tied arch, suspension, and cable stayed bridges.

Figure 1.2. Rope Access Bridge Inspection [7]

Current inspection techniques discussed above are effective, but they come with their own disadvantages. Snooper trucks are limited when load restrictions are posted on a bridge. If the restriction does not allow for heavy equipment on the deck, then other methods must be used. The boom trucks come at a disadvantage for low hanging bridges where there simply isn't enough clearance. Even on waterway bridges, the water depth may not allow for barges to enter the area and carry the trucks. For each of these machines, there are also high maintenance costs to keep them in service. Rope, though having a low service cost, requires specialized inspectors. Usually, these traditional methods require lane closures. Private and commercial traffic is then impeded which can lead to other concerns. Commercial vehicles hauling goods can slow economic growth if products are restricted from getting to their drop off location and law enforcement personnel or ambulances can be delayed when a few seconds can make a difference to saving someone's life. For many bridges, it may be the only possible way drivers can get to their destination. Other bridges may be the only crossing for many miles which causes a dramatic drop in efficiency. If lane closures were preventable, several of these issues could be avoided.

One of the greatest concerns with traditional inspection methods, along with all work place environments, is safety of the personnel. When lanes are closed, the flow of traffic is restricted. As vehicles begin to slow down and others begin to merge, the risk associated with a crash increases. According to data provided by the FHWA, in 2015, there were an estimated 96,626 work zone crashes [8]. The severity of these crashes is also a concern. As shown in Figure 1.3, severity has been broken down into three categories; injury, fatality, and property damage only (PDO). Based on these results, approximately 25,485 crashes resulted in an injured party and 642 involved at least one fatality in work

zone related crashes [8]. These trends also correlate in recent years with non-work zone crashes as seen in Figure 1.3 and Figure 1.4.

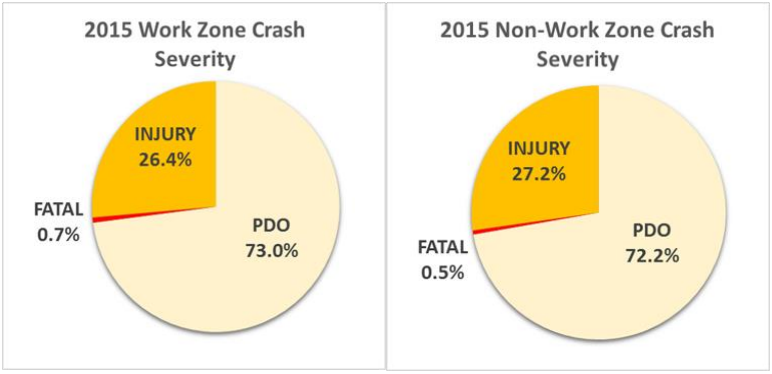

Figure 1.3. 2015 Work Zone Crash Severity [8]

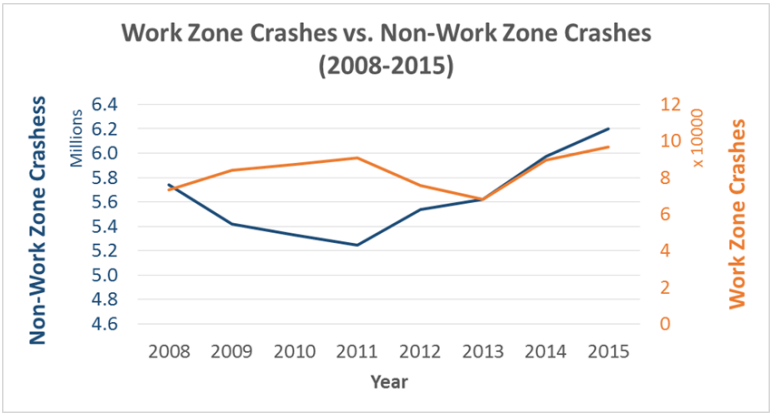

Figure 1.4. Work Zone Crashes vs. Non-Work Zone Crashes [8]

Safety of the workers and inspectors was of high priority for this research. Though fatalities have declined since 2005 due to increased safety measures and improved training techniques, road and bridge work zone fatalities still account for 1.5% to 3% of all workplace fatalities annually [8]. These fatalities are caused by a variety of reasons

involving vehicles, machinery, and improper safety measures. Climbing equipment may break while beneath the bridge and boom and snooper trucks can tilt or break while inspectors are in the bucket due to the large moment created during full extension (Figure 1.5). Health concerns also arise while inspecting below the deck due to the potential buildup of mold and fungus as well as animal droppings which typically must be disturbed and removed in order to clearly see the bridge elements. Removing bridge inspectors from these hazardous areas is the most efficient way to mitigate these risks. Using drones would allow inspectors to remain safe at a control station without placing themselves in a potentially harmful situation.

Figure 1.5. Snooper Truck Tipped Over onto Siderail [9]

1.2. RESEARCH OBJECTIVE

The objective of this research was to design a mobile platform which may be mounted with cameras and sensors to complete a thorough bridge inspection. The drone, or unmanned aerial vehicle (UAV), as designed is to be used as a tool to assist inspectors in creating detailed inspection reports while keeping personnel out of potentially dangerous

situations. To do this, special focus was placed on the current bridge inspection process so that specific scenarios could be considered. This included analyzing which elements of the bridge the drone should have access to for inspection. Federal Aviation Administration (FAA) regulations were also investigated so that the final drone design may fit within official guidelines for drone weight, pilot requirements, and more. Lab tests, field tests, and a finite element analysis (FEA) of both the overall drone and individual components were completed to minimize the drone weight yet maximize the usefulness and versatility of the mobile platform. The basis of the research began with the implementation of the drone on steel girder or stringer/multi-beam bridge systems. According to the 2017 National Bridge Inventory (NBI) Database, this main structure type accounts for 145,451 bridges, 24% of the nation's total [10]. The design will later be modified to apply to concrete bridges of this structure type which includes 85,652 bridges, an additional 14% of the bridges within the database, depending on the girder shape [10].

1.3. SCOPE OF WORK

The scope of work for this study in order to complete the objective discussed above was as follows:

- A comprehensive literature review over the bridge inspection process, FAA regulations, and drone technology which has previously been researched for the use of bridge inspections was conducted.
- A discussion over the materials used on the current design is included and materials of unknown mechanical properties were tested following proper ASTM procedures.

- A platform for bridge inspection was designed and potential benefits are addressed. A finite element analysis was performed which was used to further the design and evaluate potential areas of concern.
- Lab tests were used to confirm the feasibility of the drone design and its ability to assist with bridge inspections.
- A comparison to current technology and suggestions for future work which is recommended to be completed is also located within this report.

2. LITERATURE REVIEW

2.1. BRIDGE INSPECTION PROCESS

According to the NBIS, routine inspections, which are defined as a “regularly scheduled inspection consisting of observations and/or measurements needed to determine the physical and functional condition of the bridge, to identify any changes from initial or previously recorded conditions, and to ensure that the structure continues to satisfy present service requirements.”, are to occur at regular intervals, not to exceed twenty-four months [4]. Inspections on certain bridges may require a more frequent interval due to age, traffic, or results of past inspections. Other bridges may be allowed a larger interval, not to exceed forty-eight months, if the FHWA has given approval [4]. A fracture critical member (FCM), defined as “a steel member in tension, or with a tension element, whose failure would probably cause a portion of or the entire bridge to collapse.”, must also be inspected at a twenty-four month maximum interval but it involves a close eye, hands on inspection and possibly other non-destructive evaluation techniques [4]. Inspection procedures are located within the Manual for Bridge Inspection written by AASHTO and are also referenced by the BIRM. Common concerns noted on steel girder bridges are as follows [2]:

- Corrosion
- Fatigue Cracking
- Overloads
- Collision Damage
- Heat Damage
- Coating Failures

To locate these deficiencies, inspectors must have clear access to the bridge structure. Most defects are first detected by visual inspection; however, others may require physical means of cleaning suspected areas in order to remove paint, rust, or other debris which can hide cracks, section loss, or disturbed connections. Advanced inspection techniques allow for non-destructive testing, increasing the validity of each inspection. These methods include dye penetrants, ultrasonic testing, hardness tests, corrosion sensors, and more [2]. The BIRM mentions typical areas of the bridge which must be observed. Figure 2.1 below shows these elements, along with the typical inspection sequence.

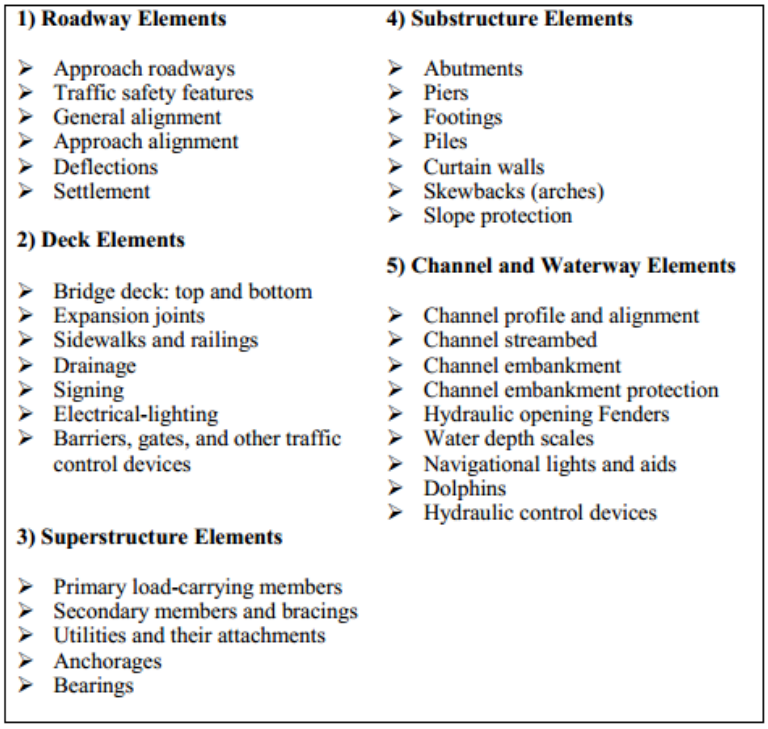

Figure 2.1. Typical Bridge Inspection Sequence [2]

For the purpose of this research, focus was placed on the superstructure elements of steel girder bridges which can later be adjusted for concrete girder systems. As discussed in the BIRM, specific locations to inspect are bearing areas, shear zones, flexure zones, and secondary members [2]. Bearing areas are those above and near the supports which resist compressive loads. Girder webs, floor beams, stringers, and stiffeners in these areas should be examined for cracks, section loss, buckling, and alignment. Shear zones, especially those near the bearing areas, also need to be inspected as these are critical areas which may contain coped members [2]. Flexure zones span between each support. Tension and compression flanges are checked for corrosion, loss of section, cracks, dings, and gouges [2]. Span splices and negative moment areas at continuous span mid-supports produce high stresses and should also be closely inspected, similarly to flexure zones [2]. Secondary members that connect main spans, including lateral bracing and diaphragms, are examined for cracked welds, fatigue cracks, loose fasteners, distortion, and corrosion [2]. Areas typically exposed to drainage are corrosion prone. Horizontal surfaces that can trap debris and moisture include the bottom flanges of girders and the pockets created by bracing connections. Structure elements may also be exposed to traffic and therefore collisions may occur. These areas are checked accordingly. The deck, superstructure, and substructure are rated based on their condition on a 0-9 scale [11]. This scale, listed in Table 2.1, is subjective and therefore requires experience to use it properly. Ratings describe the overall structure and not localized defects.

Table 2.1. Bridge Element Condition Ratings [11]

Code	Description
N	NOT APPLICABLE
9	EXCELLENT CONDITION
8	VERY GOOD CONDITION – no problems noted
7	GOOD CONDITION – some minor problems
6	SATISFACTORY CONDITION – structural elements show some minor deterioration
5	FAIR CONDITION – all primary structural elements are sound but may have minor section loss, cracking, spalling, or scour
4	POOR CONDITION – advanced section loss, deterioration, spalling, or scour
3	SERIOUS CONDITION – loss of section, deterioration, spalling, or scour have seriously affected primary structural components
2	CRITICAL CONDITION – advanced deterioration of primary structural concrete may be present, or scour may have removed substructure support. Unless closely monitored, it may be necessary to close the bridge until corrective action is taken
1	"IMMINENT" FAILURE CONDITION – major deterioration or section loss present in critical structural components or obvious vertical or horizontal movement affecting structure stability. Bridge is closed to traffic, but corrective action may put back in light service
0	FAILED CONDITION – out of service – beyond corrective action

2.2. FAA REGULATIONS

The FAA maintains control of the nation's airspace to ensure the safety and efficiency of the country's aviation system. Since 1990, the agency has allowed limited use of UAVs for disaster relief, security, and research [12]. In February 2015, a set of regulations were proposed, and later approved in June 2016, which allowed small UAVs, designated by a weight less than 24.9 kg (55 lbs), to enter the airspace for commercial purposes [12]. The approved regulation is located in the Code of Federal Regulations, Title 14, part 107, also known as 14 CFR part 107 or simply Part 107. It provides general information, operating rules, and remote pilot certification requirements. The opportunity to waiver specific regulations is also discussed in 14 CFR part 107. An aircraft which is classified as for recreational or hobby use falls under a separate regulation and was not referenced during the research process due to the design intent of the drone. The main variations between model UAV's and small UAV's regulations include the pilot licensing

and the registration process of the drone. All drones flying under 14 CFR part 107 must be registered with the FAA and must be reregistered every 3 years. A summary of part 107 including operational limitations and remote pilot in command certification is contained in Appendix A [13]. A full report of 14 CFR part 107 may be found on the Electronic Code of Federal Regulations' website [14].

2.3. INSPECTION DRONE PLATFORMS

2.3.1. Crawling & Traversing. Magnetism is commonly used as a way to connect items temporarily to a metal surface. With the assistance of mechanical devices, these magnets can also be used to create a mechanism which may allow the object to travel on the sides and bottom of a metal surface, seemly defying gravity. The Massachusetts Institute of Technology (MIT) conducted research using a crawling drone with magnetic "feet" to inspect the bottom side of a steel girder [15] (Figure 2.2). The passive magnetic feet are designed to be able to move or "walk" along the girder systems due to a tilting motion which lowers the force necessary to pull each foot away from the steel to which it is attached. Though a camera was not attached for experimentation, a "Mag-Feet" prototype was created. The initial research within the Mag-Feet thesis began with calculations applying to a planar, two-legged design, but when it came time for a functional prototype, a three-legged design was chosen in order to prevent rotational forces that occurred during motion.

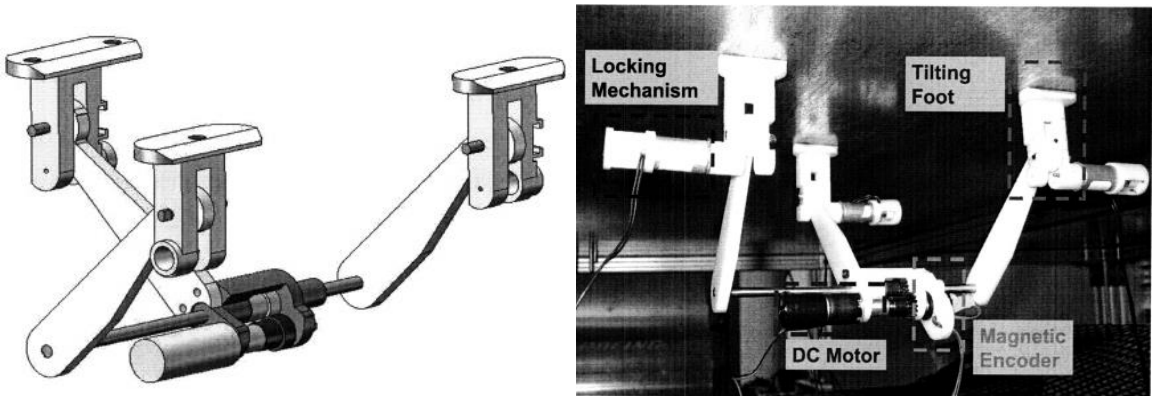

Figure 2.2. Mag-Feet Design by MIT [15]

Using a single, centralized motor, the Mag-Feet design was capable of performing three modes of gait. The “moonwalk” (Figure 2.3a), the “shuffle” (Figure 2.3b), and the “swing” (Figure 2.3c) as shown in the illustrations which describe their moment. Each gait served a purpose, but the one that vastly increased the complexity and usefulness of the design was the swing. “The goal of the swinging gait mode was to allow the robot to successfully traverse small obstacles or areas where the magnetic attachment force would be weak” [15]. The concern with the swing was that at certain swing angles, failure of the planted leg would occur. Swing angles and distances were then limited to solve this issue but resulted in decreased obstacle avoidance. With the proposed design, the drone was limited to a single plane of motion, but possible design additions were addressed which would allow a change in direction of the drone, though these were only conceptualized with the hope that they would be included in future designs. The Mag-Feet design was also limited to fairly horizontal, non-slippery surfaces. Vertical surfaces, such as beam webs, would need to be evaluated using different means due to the drone’s high center of gravity. Rust or other environmental factors which slicken the beam surface would provide a

difficult situation for the Mag-Feet due to the friction necessary to perform the tilting and sliding of the feet.

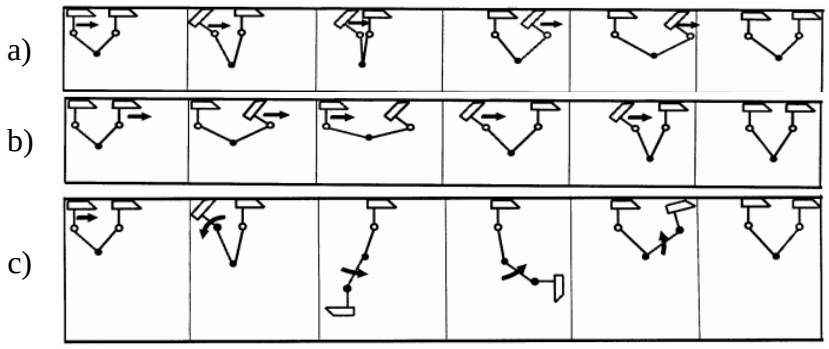

Figure 2.3. Mag-Feet Gaits:
a) Moonwalk, b) Shuffle, c) Swing. [15]

The University of Nevada, Reno, in conjunction with the University of Technology, Sydney, Australia and Duy Tan University, Da Nang, Vietnam, focused their efforts on a similar magnetic inspection robotic system, but rather than one which "walked", a drone which crawled was designed [16] [17]. The proposed system used four motorized wheels. Each of these wheels were lined with 36 Neodymium magnets to create an approximate 6 kg/wheel (13.2 lbs/wheel) capacity after being covered in a thin layer of cloth to improve the frictional coefficient between the drone and the steel surface to which it attached. This capacity allowed for an approximate payload of 7 kg (15.4 lbs). Eight servo motors were used to propel the vehicle. Four of which were used to drive the front and back sets of wheels. The second set of motors allowed the wheels to be lifted. This permitted the drone to lift itself over small obstacles and fabrication occurrences like flange splice plate connections. To maintain the design strength of the magnetic wheel system, the drone

required a steel surface which was a minimum of 20.3 mm x 28 mm (0.8 in x 1.1 in) below each wheel. Because of this and the lifting mechanism, if the robot reached a bolted collection, the drone may pass through, but only if there was the proper space between the bolt group. With a crawling drone such as this, the drone required an autonomous detection system which used infrared range sensors to scan for the edge of the structure to which it is attached. When an edge, hole, or gap was detected, a predefined algorithm then adjusted the robot's motion to a safe direction, preventing the drone from falling off the structure. With the proposed system, one 12V battery powered the camera and computer systems, while a 7.4V battery provided the energy to drive the motors. The design, shown in Figure 2.4, could be used on both horizontal and vertical surfaces due to its low center of gravity.

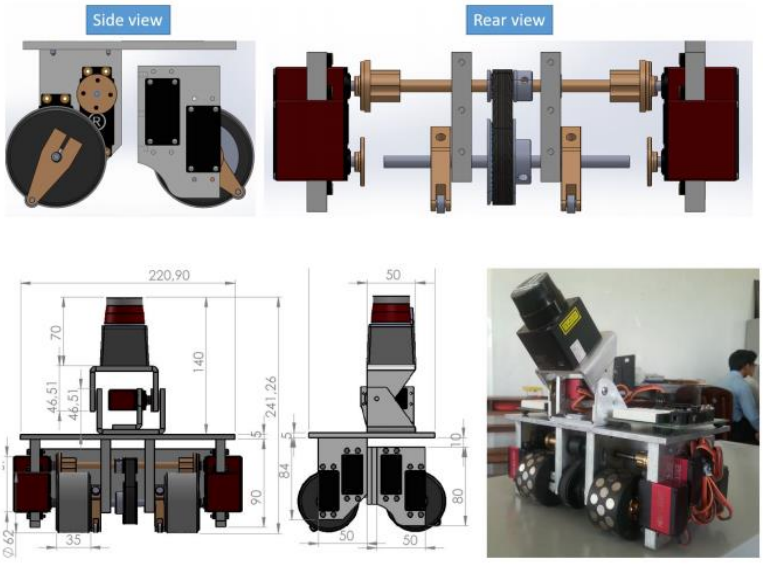

Figure 2.4. Proposed Crawling Design by the University of Nevada, Reno [16]

The above design was initially released in 2016. In 2018, an updated design was fabricated by the original creators (Figure 2.5) [18]. Though the previous papers did not specify a drone design weight, the new design had a weight of approximately 3 kg (6.61 lb) including the onboard camera systems, which was likely much lower than the previous design due to a few key changes. The size of the drone was reduced overall as shown in Figure 2.6. Rather than having eight motors to drive the drone, the new design had three motors with updated features. The ability to lift each wheel individually was removed and the wheels were converted to a track, tank-like system that only required two motors instead of four. A single centralized motor allowed for the drone to be transformed to apply towards rounded structures such as bridge columns. This design tested successfully on more than 20 different bridges with varying surface conditions (Figure 2.7). It also tested well on all surface angles. Though additional payload was not discussed within the research paper, tests and performance seem to align with an increase in drone functionality with the new design.

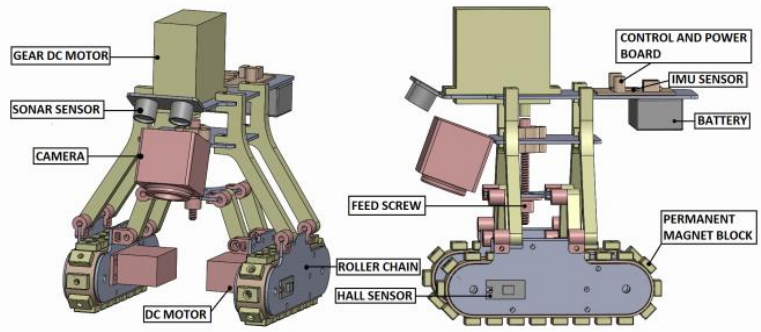

Figure 2.5. Crawling Design V2 by the University of Nevada, Reno [18]

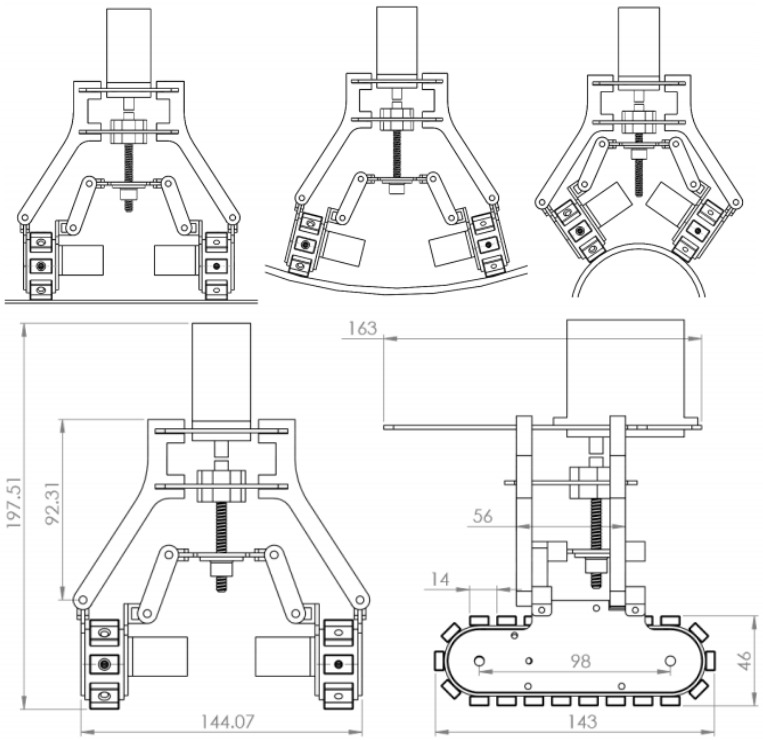

Figure 2.6. Crawling Drone V2 Dimensions [18]

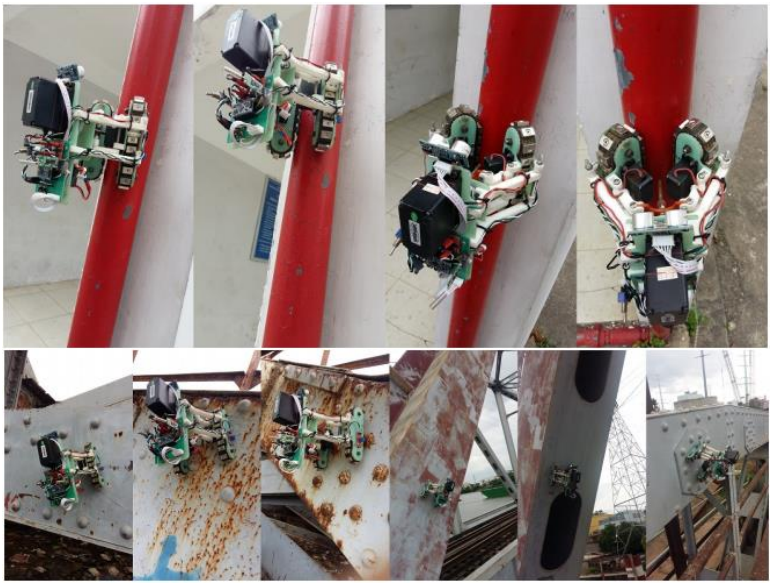

Figure 2.7. Crawling Drone V2 Field Test Structures [18]

Magnetism has its advantages, but it also comes with its own set of problems. The first is clear; the structure must be magnetic. Concrete, wood, and other structures do not apply to these designs. Magnetism relies heavily on distance, condition of the metal surface, and frictional values. That means if the force created is overcome or reduced for any reason: overturning moments from large payloads, environmental factors like wind, ice, debris, or heavily corroded surfaces, the drone could detach from the surface. This would cause almost instant and potentially catastrophic failure. Because of this, a design was conceptualized by the Center for Transportation Studies at the University of Virginia [19]. This robotic platform had three major design elements as shown in Figure 2.8. The module bodies were the main components of the drone which contained the power supply, control mechanisms, and radio equipment. The drive assemblies allowed for the attachment to the beam flanges and would give the drone the ability to traverse along the girder system. The front and back wheels attached above the flange while the middle wheel provided a vertical force to the underside of the flange adding stability and security. Each of these wheels could be independent, able to detach and reconnect as the drone encountered obstacles like shear stiffeners. This conceptual design was rather large compared to the other drones in this literature review. With an approximate length of 1.83 m (6.0 feet) and a width of 1.52 m (5.0 feet), the design spanned between two girder flanges. The module system would be placed in three separate parts due to the potential weight of the drone. In this location, the drone also needed to avoid lateral bracing located on typical steel girder construction which runs from girder to girder. Connecting the arms and wheels towards the top of the module bodies helped to avoid this. The main concerns that arose with this conceptualization were size, weight, and initial placement of the system.

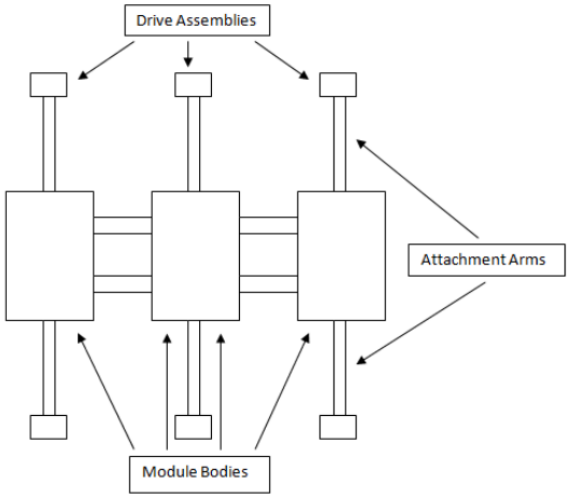

Figure 2.8. University of Virginia Drone Outline [19]

2.3.2. Unmanned Aerial Vehicles. A conference paper written by Norman Hallermann and Guido Morgenthal examined the use of a BUW Falcon Photo UAV (Figure 2.9) produced by Ascending Technologies as a bridge inspection drone [20]. Due to being released prior to FAA regulation Part 107, the drone was limited to 5 kg (11.02 lbs). Eight rotors in a V-shaped configuration gave flight capability to the drone creating a maximum takeoff weight of 2.2 kg (4.85 lbs). With built-in redundancies, failure of up to two of the motors was possible without affecting the stability of the craft. The stability, accuracy of position, and orientation of the flight system was created using eleven different sensors including accelerometers, a gyroscope, a compass, and a barometric altitude sensor. Global Positioning System (GPS) monitoring with an inertial measurement unit also allowed for stable flight in winds up to 12 m/s (26.8 mph). With a standard payload of 650 g (1.43 lbs), this drone was limited to small, compact camera attachments. With the complete system being fueled by an 8000 mAh battery pack, the UAV was designed for an estimated flight time of 18 minutes with the standard payload. Through the GPS software installed on the

BUW Falcon Photo, pre-planning of semi-autonomous flight missions were possible. The ability to create a pre-determined path using existing data allowed for automatic data acquisition which could be highly efficient by reducing the potential for locations where the cameras failed to photograph, also known as “dead zones”.

Figure 2.9. BUW Falcon Photo UAV [20]

The Minnesota Department of Transportation, with the help of Collins Engineers, Inc. chose to begin their research using the Aeyron Skyranger which cost approximately $140,000 [21]. The design, which considered military, commercial, and public safety aspects, had all-weather capability for use during rain and had the option to change payloads. Technical specifications of this drone claimed to allow for a 50-minute flight time, the ability to withstand wind gusts up to 55 mph, and a 1.9 mi integrated capability range. A 360-degree camera was installed on the Skyranger in order to view all directions during flight. Other UAV models were examined during MnDOT’s research, but they lacked the capabilities necessary to be efficient for bridge inspection, mainly flight time, processing software, and material durability. Their research was also completed prior to the approval of FAA part 107 and therefore potential UAV models had to be approved by the FAA. The submitted models were not approved in time for the project, therefore only

the Skyranger was tested. Future technologies were also discussed by MnDOT. Sensefly eXom was not yet released at the time of testing, but this drone featured the ability to look up, fly under bridge decks, and contained sensors used to avoid object collision. This model also had battery life that allowed for a 22-minute flight time and a 0.5-mile remote control range. The anticipated starting cost for the Sensefly eXom was $45,000.

The Skyranger assisted in the field inspection of four bridges, comparing previous field notes from inspectors to the results of the tests. The main problem that arose was that the drone would fly under the deck and lose its GPS signal, causing an automatic "return to home" response, sending the drone vertically into the bridge deck. A strong Wi-Fi signal was also difficult to achieve due to signal interference. Data collected by the Skyranger camera system allowed the team to view almost all the concerns noted during previous routine inspections. From this research, it was concluded that UAVs can be used safely to perform bridge inspections. They proved to be more suitable for larger bridges but need the ability to direct cameras and have the capability of flying without a GPS signal.

Dr. Jennifer Bridge and Peter Ifju of the University of Florida completed their study by not only creating the design of a drone, but also implementing field tests, side by side with bridge inspectors using traditional inspection techniques [22]. Figure 2.10 shows the aerial drone created for their study. The choice was made to design a UAV rather than purchasing a commercial one off-the-shelf which was not built for the purpose of under bridge inspections. Features which were deemed necessary included the ability to fly without GPS technology which would likely be lost under the bridge deck, the ability to sufficiently carry large and various payloads, stable flight capabilities, and precise flight maneuverability. A quadcopter design was chosen because it typically has greater

maneuverability than a hexacopter according to the study. A camera was mounted above the drone for maximum visibility along with a laser range finder for position control and crash avoidance. The camera could be independently controlled using a servo motor but, due to the brush motors chosen for the rotor system, the video tended to be shaky. Brushless motors would have increased stability, but also increased weight, therefore decreasing flight time and payload. Even without stabilization, the camera provided enough clarity for inspectors to spot deficiencies. An optical flow sensor, similar to those found in wireless computer mice, was used to track positioning. The sensor was faced upward at the bridge deck rather than down below where water passing beneath the bridge could affect position. This sensor allowed the drone to automatically hold its position while the camera could be rotated to examine the bridge structure. Unlike the other drones discussed in this literature review, Dr. Bridge and Ifju also examined the concern of "what if it crashes". Since the bridges examined in the study were over water, the landing gears were retrofitted with polyethylene foam to increase the buoyancy of the vehicle. This also provided a dampening effect if the drone were to crash on a hard surface.

Figure 2.10. Dr. Bridge et al. Inspection Drone Design [22]

Eight bridge inspections throughout north Florida were conducted using the University of Florida's design; three of which were alongside scheduled routine bridge inspections [22]. Design concerns noted during the inspections were stability difficulty due to wind gusts and the optical flow sensor had difficulty picking up enough reference points to maintain location. Final results included inspector's and Florida Department of Transportation's spectator feedback through a set of questions for a total of 16 responses. Data showed that the overall rating of the drone compared to traditional inspection methods were average to above average. Figure 2.11 shows the response data on whether UAV inspections should be adopted. Constructive criticism applicable to this research thesis that was gathered included longer flight times and the need for increased flight stability underneath the bridge. Recommendations were also made for determining a way to view the top face of the bottom flanges of steel girders. The use of a standard UAV also made it impossible to view deterioration that was covered by debris. It was suggested that the best application for UAVs was for inspections on bridges previously established as being in good condition.

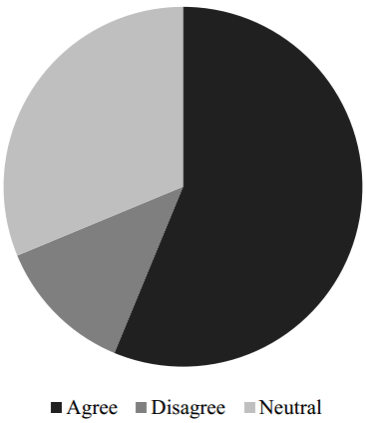

Figure 2.11. Response Data for Whether UAV Inspections Should be Adopted [22]

2.3.3. Feasibility Studies & DOT Implementation. Some of the studies above, including a few others to be discussed below, decided to look more into answering the question "is using a UAV to improve bridge inspections feasible?" This included logical assessments, costs assessments, current states' DOT implementation, and bridge inspector question surveys.

Prior to the release of the research above by Morgenthal and Hallerman, a portion reprinted from "Advances in Structural Engineering" in 2014 under the same authors also addressed the use of a flying drone for bridge inspections [23]. This research did not focus as much on the design of the drone, but more the feasibility, with motion blur of the drone being the main concern of the study. This was related directly to the drone platform and its positional stability. It was concluded that camera systems with complex algorithms could sufficiently collect crack data and locations, even with motion blur. What was not mentioned was how an improved camera system and increased in-flight computing power would affect the overall UAV weight, potentially decreasing additional payload. Morganthal and Hallerman deduced that UAVs have the advantages of being much smaller and more portable than tradition inspection methods. They can also be used in high risk situations where bridge damages may endanger human life. Limitations mentioned included very small payload capabilities, short flight times, sensitivity to weather conditions, and the need for well-trained, experienced pilots. Flight permissions can also limit feasibility due to line of sight requirements and restricted flight zones.

Griffith University located in Australia focused their efforts in 2015, not on the drone itself, but the laws and costs associated with the inspection process and flight regulations [24]. Though flying under the Civil Aviation Safety Authority of Australia

rather than the FAA, many of the findings and conclusions still apply. Chan et al. performed a case study on a two-span deck unit bridge in Queensland. The structure had two lanes with no shoulder, so a lane closure would require traffic to stop and enter the opposing lane. Traffic control was then utilized for 3.5 hours with the inspection of the substructure and superstructure amounting to two hours. A cost analysis was performed, resulting in Table 2.2. Several assumptions were made in the creation of the table below. Use of a UAV would not require the use of an underbridge inspection unit which caused a huge variation as shown. The cost of a UAV over a predicted drone lifespan was not included. Without mobilization of equipment, 1.5 hours were predicted to be saved within the case study, decreasing the cost of the two inspectors performing the inspection. Minimal traffic control was still included due to flight regulations not allowing the drone to fly above traffic, therefore brief traffic disruption would be necessary.

Table 2.2. Basic Cost Comparison for Inspection Disbursement

Inspection Disbursement	Manual Inspections	UAV Based Inspection
Traffic Control	$640	$320
Underbridge Inspection Unit	$2000	-
Bridge Inspectors	$1200	$750
TOTAL	$3840	$1070

Chan et al. discussed several limitations which occur with a UAV [24]. If the bridge is an overpass, with laws similar the FAA regulations, traffic must be halted beneath the bridge to perform the inspection, increasing the need for traffic control. Bridge structures themselves also provide a hindrance due to visual line of sight requirements. As the drone

passes between girders or around pier elements, line of sight is lost. Maneuvering around these obstacles require highly trained pilots rather than the typical bridge inspectors unless they are subjected to many hours of training. The drone also needs to have fail-safe programing for crash avoidance which adds weight and lowers the potential for additional payload. These systems can also greatly increase the cost of the drone, decreasing the financial benefits. The group concluded that there is a significant potential for the use of drones in bridge inspections, but operational and regulatory requirements hinder widespread deployment of UAV systems.

The concept of using drones for bridge inspections has expanded rapidly since the release of 14 CFR part 107. A final project report released by Oregon State University in 2016 discussed "Cost-Effective Bridge Safety Inspection Using Unmanned Aerial Vehicles (UAVs)" [25]. This study was aimed at creating a detailed literature review of the use of UAVs in bridge inspections, particularly those performed by state's department of transportation (DOT). Table 2.3 below shows the state DOTs which had been researching drone usage at the time of the study. Those states which had been specifically studying bridge inspections included Connecticut, Florida, Michigan, and Minnesota. Types of "other applications" discussed included investigating roadway slope stability, digital surface models, and avalanche monitoring and control. Regarding the applicability of UAVs for bridge inspections and the items that can be aided by drones, the tables found in Appendix B were created. Note that the researchers chose to refer to UAVs as unmanned aerial systems (UASs) which encompassed both the UAV and the ground control station for piloting the drone.

In March of 2016, AASHTO released a study which increased the number of state DOTs which have researched or used drones to 17 [26]. These include, Alabama, Connecticut, Delaware, Idaho, Indiana, Kentucky, Maryland, Massachusetts, Minnesota, Michigan, New York, Ohio, Oregon, South Carolina, Tennessee, Vermont and Washington. 16 others said that drones were being considered, but not yet implemented including some of those listed in Table 2.3. In the news release, research performed by the Minnesota Department of Transportation was mentioned which estimated that "a standard bridge deck inspection takes eight hours, a crew of four people and heavy equipment, costing at an estimated $4,600. The same inspection with a drone takes two people just two hours at an estimated cost of $250." [26].

Table 2.3. Example Usage of UAVs in Various DOTs [25]

DOT	Traffic Monitoring	Structural Inspection	Construction Site Inspection	Other Applications
Arkansas	X			
California				X
Connecticut		X		
Florida		X		
Georgia	X			
Michigan	X	X		X
Minnesota		X		
North Carolina				X
Ohio		X		X
Texas				X
Utah			X	
Washington	X			X
West Virginia	X		X	

3. MATERIALS AND METHODOLOGY

3.1. MATERIALS

3.1.1. Carbon Fiber. Carbon fiber is a directionally dependent material, also known as anisotropic [27]. The most common material with similar characteristics is wood. Wood grains run longitudinal along a piece of lumber which create an increase of strength in this direction. Therefore, the strength of a piece of lumber is dependent on the orientation of the wood grain. Carbon fiber composites, created using fibers and a resin, produce similar results by having strength characteristics which can be varied by the orientation of the fiber. These fibers can be unidirectional, having been placed in clearly defined directions, or chopped and multidirectional, which create a seemingly global isotropic material, having the same properties in all directions, while local properties are still dependent on the fiber direction.

Due to the built-up nature of carbon fiber laminates, the volume of fiber and resin are highly variable to help create the necessary material properties for specific design applications. The ratio between the components effect longitudinal and transverse strength, Poisson's ratio, elastic and shear moduli, and material density. MatWeb.com had created a database which showed the typical range and average for each carbon fiber material property. The properties necessary for FEA simulations are shown below in Table 3.1.

1/4-inch thick sheets of standard carbon fiber laminate, produced by Clearwater Composites, LLC, were used for flat components of the drone prototype to determine product feasibility. Clearwater Composites defined the material used as "Standard Modulus" with a unidirectional 0°/90° balanced layout so that material properties were

equal in perpendicular directions. Properties provided by Clearwater Composites, LLC, are shown in Table 3.2. Composite parts were precision cut from a larger sheet and cut edges were monitored for flaws which could induce a stress concentration. Due to carbon fiber's high strength to weight ratio, it became a common material for UAV applications.

Table 3.1. Typical Carbon Fiber Composite Properties [28]

Property	Range	Average
Elastic Modulus	2.62-520 GPa	102 GPa
Poisson's Ratio	.02-.90	.433
Shear Modulus	1.93-5.60 GPa	4.30 GPa
Mass Density	1.15-2.25 g/cc	1.43 g/cc
Tensile Strength	0.917-3790 MPa	901 MPa
Compressive Strength	50-1740 MPa	78.1 MPa
Yield Strength	4.62-2650 MPa	1080 MPa

Table 3.2. Properties of ¼" Clearwater Composites Carbon Fiber Laminate [29]

Property	Value
Elastic Modulus	62 Gpa
Poisson's Ratio	0.02
Shear Modulus	3.58 GPa
Mass Density	1.55 g/cc
Tensile Strength	1030 MPa
Compressive Strength	--*
Yield Strength	--*

*Data not provided by Clearwater Composites

3.1.2. Markforged Onyx. The material known as Onyx, created by Markforged, was their newest filament created as an alternative to their standard Tough Nylon product for 3D printing [30]. It was characterized by its hardness, surface finish, and layer adhesion. Onyx was composed of an engineering nylon matrix with a chopped carbon fiber structural reinforcement. This reinforcement allowed Markforged to market the material as being 3.5 times stiffer than their standard nylon [30]. The combination of the matrix and chopped

fiber also allowed the material to have high wear resistance and engineering toughness [30]. If the application requires the material to have more strength, it could also be reinforced with continuous high-strength fibers like carbon fiber, Kevlar, or fiberglass [30]. Onyx, due to its composition, had dimensional stability and a clean surface finish [30]. This meant that during 3D printing, minimal warping caused by a cooling gradient would occur on the print bed and there was no need for surface treating or cleaning to remove a rough surface and sharp edges. The datasheet provided in Appendix C contains the material properties which were given by Markforged [31]. The decision to use Onyx was related to its functionality. A 3D printed material allows for a wide range of production capabilities. For the UAV design, weight was of high importance. Aluminum has a density of 2.78 g/cm^3 (0.1 lb/in^3) with a tensile strength of 75.8 MPa (11 ksi) giving a tensile strength to weight ratio of approximately 27.3 Nm/g (110 $ksi/(lb/in^3)$) [28]. Onyx, however, with a density of 1.18 g/cm^3 (0.043 lb/in^3) and an advertised tensile strength of 36 MPa (5.2 ksi), had a tensile strength to weight ratio of approximately 30.5 Nm/g (121 110 $ksi/(lb/in^3)$) [31]. Having a similar strength to weight ratio to aluminum with the increased versatility makes 3D printed Onyx an ideal material for connections and non-typical structural shapes on UAV applications.

All drone parts and lab test specimens were printed using a Markforged Mark Two. Specified printer settings are located in Table 3.3. Each of these values were chosen as a starting point for testing purposes. If the material application needed more strength, settings could be changed, and material properties found in Section 4.1 could be reevaluated. The triangular infill pattern shown in Figure 3.1 was specifically chosen due to a triangle's inherent structural stability while reducing the amount of material used on the drone.

Table 3.3. Markforged Mark Two Printer Settings

Setting	Value
Fill Density	50%
Fill Pattern	Triangular
Layer Height	0.1 mm
Roof and Floor Layers	4
Wall Layers	2
Print Temperature	275 °C

Figure 3.1. 3D Printed Triangular Infill

3.2. METHODOLOGY

3.2.1. Drone Design Considerations. For the design of an inspection drone, there were various concerns that needed to be addressed. These came from all sources and were each carefully considered. The governing factor to consider was the purpose of the drone. In the case of this research, the drone would be used on singular or multi span, steel or concrete girder bridges with an I-shaped girder system. It would be required to reach below the deck in all locations to reduce, or even remove, the need for traditional inspection methods. Since the drone was to replace current inspection techniques when applicable, it needed to show a strong advantage in making the switch to this new inspection method. Therefore, it was considered that the drone needed to eliminate, or nearly eliminate, the need for lane closers. This would allow traffic to

freely move while still performing the full inspection of the superstructure. The use of the drone must also increase the safety of the inspectors when compared to current inspection practices. This meant there should be very little need for the inspectors to leave the safety of the ground when using the drone. The drone shall be capable of performing the entire inspection within its capabilities without the need for inspectors to hang over or climb under the bridge to attach the vehicle or move it around common obstacles. Speed and data clarity also needed to be analyzed if it was to replace the hands-on inspections performed by the personnel. Labor is often one of the highest costs on a project, therefore if the inspection could be performed faster and more efficiently without the use of a drone, then the drone platform would become a hinderance rather than an enhancement for the inspections performed.

FAA regulations were also considered. To remain within FAA 14 CFR part 107, the drone was kept below 24.9 kg (55 lbs). This included the self-weight of the vehicle and any additional payload added to the drone during flight. Since this research focused on the design of an inspection platform, it was critical that the structure be light and structurally efficient in preparation for the unknown payload the drone may carry. The drone must also remain within the line-of-sight of the operator during its flight at a close enough range to clearly view its location without the need for vision aid devices like binoculars. The aircraft must also not fly above any person not directly participating in the operation. This was especially a concern when dealing with bridge overpasses.

As mentioned, the drone design was intended to be used on steel and concrete girder bridges and therefore fabrication techniques were reviewed. Figures 3.2 and 3.3 below were a few of the concerns which affected the drone design. These included variable depth girders (Figure 3.2), variable flange widths, lateral bracing, and curves (Figure 3.3).

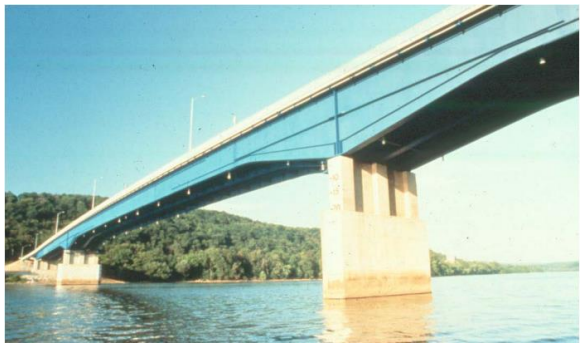

Figure 3.2. Fabricated Variable Depth Girder Bridge [2]

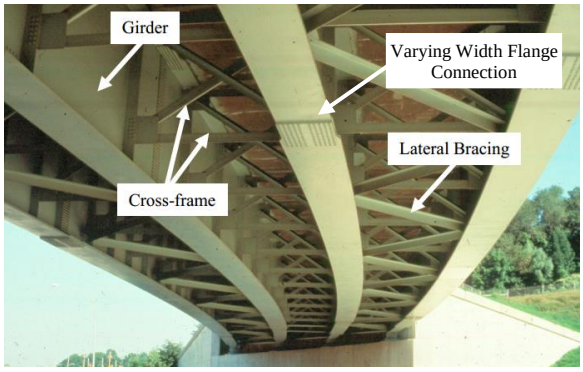

Figure 3.3. Curved Multi-Girder Bridge [2]

For concrete structures, specifically those constructed using I-beams and Bulb-Tee Beams as shown in Figure 3.4, similar conditions to those of steel girder bridges were apparent. Flange connection plates as shown in Figure 3.3 were not found on

concrete bridges, but lateral bracing, varying flange widths, and variable girder depths were present depending on the design and construction method. The concrete beams did provide a new situation, this being the introduction of sloped flanges which were not present in steel girder construction.

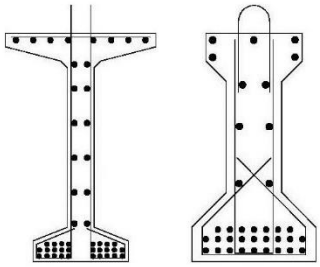

Figure 3.4. Common Concrete Girder Types:
Concrete Bulb-Tee Beam (Left), Concrete I-Beam (Right) [32]

Flight duration was also a variable when studying the drone feasibility and efficiency. An optimal relationship between flight duration and potential payload needed to be determined to benefit the inspector. If the drone could carry a large payload, and therefore more equipment, the effect may be a much shorter flight time and therefore the inspection could not be completed without multiple battery replacements or charging. The opposite end of the spectrum was a scenario where the drone had a large enough power source to complete a large inspection process, but at the expense of only being able to carry small and lightweight equipment. A feasible design allowed for a battery life capable of completing an average inspection while carrying expected inspection equipment.

The final design intent was for the data collected by the drone to be sent back in real time to the inspector. Inspectors are often traveling from one bridge to the next within the same day. If data is not processed on site, personnel may be hours away from the jobsite, especially if it took several days to review the data. If there is a concern or a problem with data collection, inspectors may need to revisit the site for further investigation. A need to return to a previously completed inspection site would increase labor hours and cause a major delay on other scheduled site visits. Data in real time allows for instant feedback to the inspector. If there is a concern which needs further review, the personnel are already on site and available to check the specific location.

3.2.2. Onyx Material Testing. To determine the material properties necessary to complete a FEA on the UAV, it was necessary to determine Onyx's elastic modulus, Poisson's ratio, shear modulus, tensile strength, compressive strength, and yield strength. Values provided by Markforged in Appendix C could not be taken directly due to the 50% triangular infill print pattern. These properties were determined using American Society for Testing and Materials (ASTM) D3039, D6641, and D7078

3.2.2.1. ASTM D3039 – tension. ASTM D3039 "Standard Test Method for Tensile Properties of Polymer Matrix Composite Materials" was used to determine ultimate tensile strength, yield strength, and Poisson's ratio [33]. Before beginning the test, coupon type and geometry were determined. Table 3.4 below are geometry recommendations provided by ASTM D3039.

Table 3.4. Tensile Specimen Geometry Recommendations [33]

Fiber Orientation	Width, mm [in.]	Overall Length, mm [in.]	Thickness, mm [in.]	Tab Length, mm [in.]	Tab Thickness, mm [in.]	Tab Bevel Angle,°
0° unidirectional	15 [0.5]	250 [10.0]	1.0 [0.040]	56 [2.25]	1.5 [0.062]	7 or 90
90° unidirectional	25 [1.0]	175 [7.0]	2.0 [0.080]	25 [1.0]	1.5 [0.062]	90
balanced and symmetric	25 [1.0]	250 [10.0]	2.5 [0.100]	emery cloth	—	—
random-discontinuous	25 [1.0]	250 [10.0]	2.5 [0.100]	emery cloth	—	—

Onyx was considered a random-discontinuous fiber orientation and therefore specimens were printed with the recommended geometry. Tabs, ends which are thicker than the central gage area, were not directly required for the fiber orientation. They may be implemented if specimen failure occurred near the grips (<1 specimen width), but this issue did not occur as shown in the results. To determine the area of each printed specimen, width and thickness measurements were taken at three locations and averaged. In order to be determined as valid, width tolerance was required within 1% (±0.25 mm (±0.01 in)) of the intended value and thickness was required by ASTM D3039 to be within a 4% tolerance (±0.1 mm (±0.004 in)). The tensile specimen used is shown in Figure 3.5.

Figure 3.5. Tensile Specimen

Strain values were necessary to determine the material's modulus of elasticity and Poisson's ratio. Strain gages with a 12.7 mm (0.5 in) active gage length and a 350-ohm resistance were chosen to collect strain data during the experimentation process. A large

active gage length was chosen due to the triangular infill pattern. It was determined to be necessary that the gage crossed multiple internal cells to provide a global strain value, rather than localized strain within each cell. A low excitation voltage was used as ASTM D3039 recommended voltages between one to two volts to prevent heating of the coupon which may affect localized performance. Strain gages were then attached to the specimens.

"When determining modulus of elasticity, it is recommended that at least one specimen per like sample be evaluated with back-to-back axial transducers to evaluate the percent bending" [33]. Percent bending was used to determine system alignment. If percent bending was less than 3% as determined by Equation 1 at approximately 2000 με, transducers need only be placed on one side of the specimen. If percent bending was greater than 3%, strains may be taken as the average of back-to-back gages on each side of the specimen. Since Poisson's ratio was also to be determined, strain gages were placed in the transverse direction as required. Strain data was collected at a sampling rate of two per second by a data acquisition system.

$$B_y = \left|\varepsilon_f - \varepsilon_b\right| / \left|\varepsilon_f + \varepsilon_b\right| * 100 \quad (1)$$

The specimen was inserted into an Instron 5965 (Figure 3.6) with careful consideration to align the sample with the machine to induce pure axial stress. A folded strip of fine grit emery cloth was used between the grips and the specimen to provide a non-slip surface and prevent damage to the sample as describe by ASTM D3039. Grips were tightened to restrict movement, but not to create addition stresses and induce premature specimen failure at the grip location. Since manual grips were used, pressure was not recorded as recommended by the standard.

A constant head speed tension test was performed at a rate of 8 mm/min to allow for a specimen failure between one to 10 minutes. At this rate, and due to the elasticity of the material, strain gage failure would occur prior to the completion of the test, but sufficient data was collected to produce strain diagrams and determine the necessary properties as shown in Section 4.1. Load and extension data were collected by the Instron Bluehill 3 testing software at a rate of two per second to align with the strain capture rate.

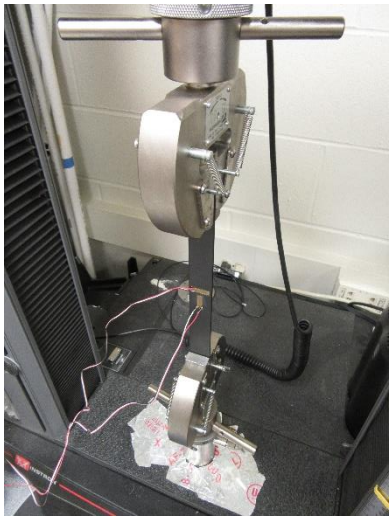

Figure 3.6. Tension Test Compete Setup

3.2.2.2. ASTM D6641 – compression. Ultimate compressive strength was determined using ASTM D6641 “Standard Test Method for Compressive Properties of Polymer Matrix Composite Materials Using a Combined Loading Compression (CLC) Test Fixture “ [34]. Loads from the Instron 5965 are transferred to the specimen through both shear and end loading through the fixture shown in Figure 3.7. The gage length was adjusted to 12 mm (0.46 in) and a recess for an extensometer was not used. Each of these modifications are allowed within ASTM D6641 limitations.

In order to determine the specimen geometry, several trials were performed to validate the test. For the first round of validation, samples were printed using the recommended starting values for an untabbed specimen (Table 3.5). Two requirements must be met for the test results to be conclusive. The first was that failure must occur within the gage length. End crushing or delamination within the grips may not provide a proper representation of the compressive strength of the material. Euler buckling within the gage length must also be limited as this could cause decreased ultimate compressive load values. Having a small unbraced gage length in relation to the specimen thickness improved the chances of forcing pure compression and preventing buckling from occurring.

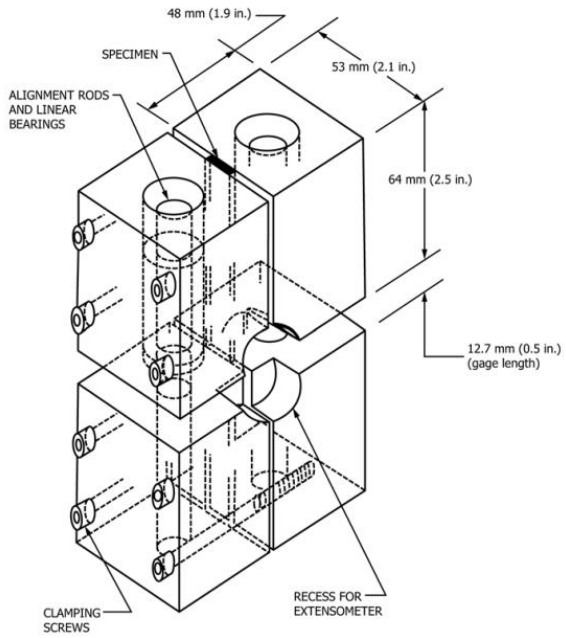

Figure 3.7. ASTM Recommended CLC Test Fixture [34]

Table 3.5. Recommended Compression Specimen Geometry [34]

Dimension	Value
Height	140.0 mm (5.51in)
Width	13.0 mm (0.51in)
Thickness	2.5 mm (0.10in)

Beginning with the recommended values as shown in Table 3.5, 3 mm (0.12 in) active gage length, 120-ohm resistance strain gages were chosen to collect strain data during compression testing. It was necessary for these gages to be smaller than the tensile test to fit within the 12 mm specimen gage length. These gages were places on each side of the specimen as required by ASTM D6641 in order to check for Euler Buckling for a minimum of five samples. One gage may be used for the number of specimens greater than five.

To begin the test, the specimen was placed in the testing fixture following the ASTM procedure. Section 11.2.7 of D6641 stated to torque all eight of the clamping screws to 2.5-3.0 N-m (20-25 in-lb). A dial torque wrench was used and torque was applied in three increments from zero to 1.13 N-m (10 in-lbs), then 1.69 N-m (15 in-lbs), until reaching approximately 2.60 N-m (23 in-lbs). These torques were applied in a diagonal pattern across the bolts to allow for an even stress distribution across the specimen. If the torque was too low, the shear friction against the specimen may fail causing end crushing [34]. If it was too high, stress concentrations would build at the ends of the gage sections and lead to a premature failure [34]. The adequacy of the clamping force was dependent on the material, so it was important to watch for these concerns. The fixture was then placed centrally within the Instron 5965 as shown in Figure 3.8 and strain gauges were attached to the data acquisition system. Similarly to

the tension test, failure was suggested to occur within one to 10 minutes. For this reason, a constant head test speed of 1.0 mm/min (0.039 in/min) was chosen with data being collected at a rate of two per second.

As discussed earlier, the test was validated if end crushing or other failure types within the grips did not occur, along with a limited amount of Euler buckling within the gage length. Strain gages on either side of the specimen are compared using Equation 1 shown previously in Section 3.2.2.1. It was discussed in ASTM D6641 that strain bending was to be limited to less than 10% at a strain value of approximately 2000 με which was the middle of the range used to determine the compressive chord modulus (approximately 1000 – 3000 με). Bending must also be limited at the point of ultimate strength.

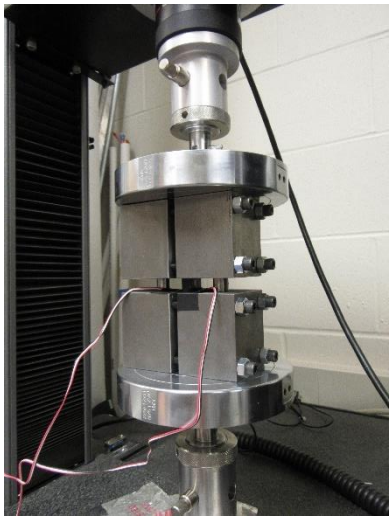

Figure 3.8. Compression Load Test Setup

Using the recommended geometry from Table 3.5, there was a very strong presence of visual buckling as shown in Figure 3.9. For this reason, the size of the

specimen was increased until the final dimensions shown in Table 3.6. These dimensions gave adequate percent bending results as discussed in Section 4.1.2.

Figure 3.9. Recommended Geometry Visual Buckling

Table 3.6. Final Compression Specimen Dimensions

Dimension	Value
Height	140 mm (5.51in)
Width	21 mm (0.83in)
Thickness	7 mm (0.28in)

3.2.2.3. ASTM D7078 – shear. The procedure for the shear test may be found in ASTM D7078 “Standard Test Method for the Shear Properties of Composite Materials by V-Notched Rail Shear Method” [35]. This method, as it related to Onyx, was for testing “short-fiber-reinforced composites with a majority of the fibers being randomly distributed” among other material types [35]. From this test, the objective was to determine the shear chord modulus of elasticity. The size of the printed specimen is shown below in Figure 3.10 with dimensions listed in Table 3.7. A thickness of 4 mm (0.16 in) was chosen for the specimen due to ASTM suggesting a thickness between 2 – 5 mm (0.080 – 0.200 in) in ASTM D7078 Section 8.2.2.1.

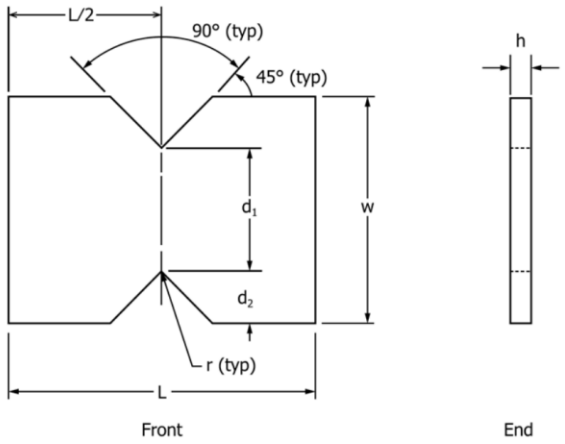

Figure 3.10. Shear Specimen [35]

Table 3.7. Shear Specimen Dimensions [35]

Dimension	Value
d_1	31.0 mm (1.22in)
d_2	12.7 mm (0.50in)
h	4.0 mm (0.16in)
L	76.0 mm (2.99in)
r	1.3 mm (0.05in)
w	56.0 mm (2.20in)

A minimum of five specimens were required to be tested, therefore seven tests were completed to determine the shear modulus. Since shear force was concentrated within the notch, the cross-sectional area of each specimen was taken at this location. 120-ohm, 3 mm (0.12 in) active gage length strain gauges were used to determine the shear strain. These were placed in a ±45° pattern to the load direction, spaced centrally between the notches (Figure 3.11). Two gages were placed on each side of the specimen. ASTM D7078 Section 6.4 discussed force eccentricity and its bending effect on the specimen. Percent twist was to be evaluated at 0.004 engineering shear strain and a result greater than 3% was to be examined for possible reasons. If no cause was apparent, shear modulus was to be

calculated using the average response of back to back specimens. It was chosen to examine the average result of each test to minimize error and therefore percent twist was not evaluated.

As with the other material tests, ASTM D7078 specified for failure to occur within one to 10 minutes, therefore a constant head-speed test was performed at a rate of 1 mm/min (0.04 in/min). Following the procedure in ASTM 7078, the specimen was loaded into the first half of the testing fixture shown in Figure 3.12. Bolts were recommended to be torqued to 55 N-m (40 ft-lb) by the standard. It was determined that this was a far higher torque than necessary to prevent slippage of the specimen within the grips as ASTM D6641 used a torque of 2.60 N-m (23 in-lbs) without slippage. Damage to the specimen due to excessive grip pressure may lead to premature failures and therefore a torque of 4.52 N-m (40 in-lb) was used for this experiment.

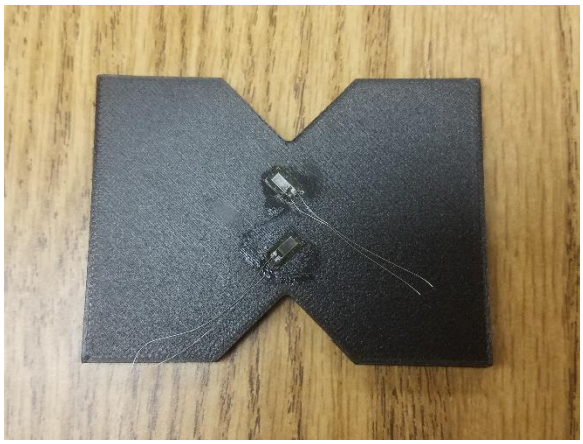

Figure 3.11. ±45° Shear Strain Gages

Figure 3.12. Shear Test Fixture

Strain gages were then zeroed using the data acquisition system before inserting the specimen into the second half of the fixture to capture any strain bending resulting from the complete test set up. The shear fixture was then placed in the Instron machine (Figure 3.13) and the constant head-speed was performed. Data was recorded at a rate of two readings per second as suggested by ASTM D7078. Failure should occur within the gage section and not at the point of an obvious specimen flaw.

Figure 3.13. Complete Shear Test Setup

3.2.3. Drone Experimentation. After the formation of a drone prototype, the drone was subjected to two types of experimentation: FEA simulations and laboratory testing. FEA simulations allowed the designer to see and evaluate the load path throughout the model. This was used to determine points of high stress concentration so that they may be assessed for potential failure or large deflections. In order to perform the simulations, the average material properties found during material testing and typical properties found through research were used. By using the average and typical values of non-tested materials, rather than those specific towards the material used in this research, the results were more generic and allowed for future fabricators to use materials available to them, without vastly changing the results of the simulation.

Laboratory testing was performed in order to create a controlled and safe environment for the prototype. Each test was created in order to simulate real world inspection scenarios, including proper beam flange size and beam obstacles. Laboratory experiments allowed a close eye inspection of the drone for points of failure which may have not been detected by FEA simulations. This also allowed for the safety of the drone overall so that these issues could be addressed before full scale testing where a minor failure could result in a crash and the complete loss of the drone. Full scale testing was not yet completed for this research due to the ongoing lab experimentations, therefore, full-scale testing will be discussed within Section 5.2.

4. RESULTS AND DISCUSSION

4.1. ONYX MATERIAL PROPERTIES

4.1.1. Tension Test. Following the methodology described in Section 3.2.2.1, seven tension tests were performed. To be considered valid, the majority of specimens were required to fail within the acceptable gage described as being greater than one width from the machine grips. Failures must also not occur at any obvious material flaw. As mentioned in the standard, percent bending must be calculated on a minimum of one specimen to determine the system alignment using Equation 1. Sample #2 was tested for bending with results shown in Table 4.1. Due to results being less than 3%, strain gages were placed on a single side of the remaining specimens.

Table 4.1. Tension Percent Bending Results

	Strain 1 (Front)	Strain 2 (Back)	Percent Bending
Sample #2	2038.7 με	2096.4 με	1.4%

Only five valid tests are required by ASTM D3039. Of the seven samples, Sample #1 was removed from the dataset due to failure near the grip location. Sample #5 was also removed. This sample resulted in a Poisson's ratio above 0.5 which is typically the upper limit for isotropic materials [36]. Though the test specimen was not perfectly isotropic, it was chosen to remove this sample from the dataset, assuming there was a failure in the collection of strain readings. Stress vs. strain plots from zero to approximately 10,000 με of valid specimens are shown in Figure 4.1. Strain gage failure seemed to occur soon after

10,000 με, preventing strain at total failure from being determined. This was not required for the necessary calculation and therefore was not a concern. All calculations are performed using stress vs. strain data less than 10,000 με. Parabolic trendlines describing the data are located in Table 4.2. Pearson's R value, also known as the Pearson Product Moment Correlation, is also shown. This value describes the accuracy of the equation with a value of "1" being an exact match to the dataset.

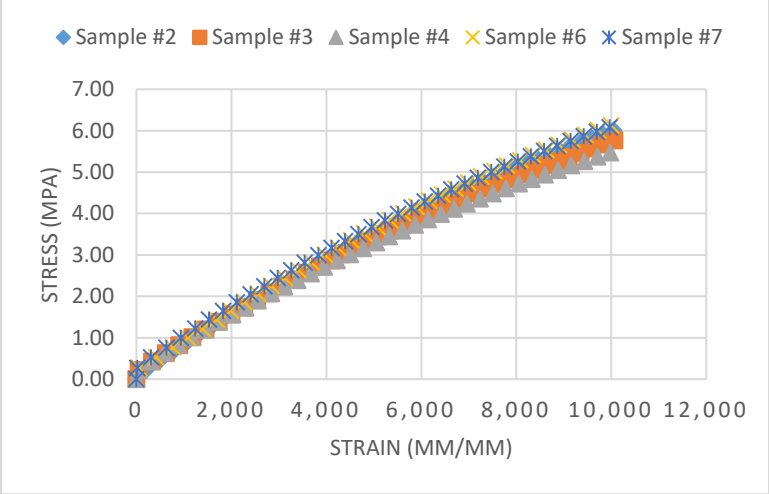

Figure 4.1. Tension Test Stress vs. Strain Results

Table 4.2. Trendline Equations for Tension Results

Sample	Equation	R^2
#2	$\sigma = -2E\text{-}08\varepsilon^2 + 0.0008\varepsilon + 0.0792$	1
#3	$\sigma = -2E\text{-}08\varepsilon^2 + 0.0007\varepsilon + 0.1909$	1
#4	$\sigma = -2E\text{-}08\varepsilon^2 + 0.0007\varepsilon + 0.2160$	1
#6	$\sigma = -2E\text{-}08\varepsilon^2 + 0.0008\varepsilon + 0.1812$	1
#7	$\sigma = -2E\text{-}08\varepsilon^2 + 0.0008\varepsilon + 0.2767$	1

Using these results, Equations 2-5 were performed to determine Onyx's Young's modulus, Poisson's ratio, tensile strength, and yield strength. Yield strength was

determined using the 0.2% offset method which states that the yield strength of a material is based on a 0.2% strain offset of a line on the stress vs. strain plot which has a slope equal to the modulus of elasticity. The yield strength was then described as the point of intersection between the linear line from Equation 5 and the trendline of the dataset for each experiment.

$$E^{chord} = \Delta\sigma_l / \Delta\varepsilon_l \tag{2}$$

$$\nu = -\Delta\varepsilon_t / \Delta\varepsilon_l \tag{3}$$

$$F^{tu} = P^{max} / A \tag{4}$$

$$\sigma_l = E(\varepsilon + .002) \tag{5}$$

Data required for FEA simulations is shown in Table 4.3. The average of the samples used for analysis was calculated using Equation 6. Standard deviation and coefficient of variation are also provided using Equation 7 and Equation 8.

$$\bar{x} = (\sum_{i=1}^{n} x_i)/n \tag{6}$$

$$S_{n-1} = \sqrt{\sum_{i=1}^{n}(x_i^2 - n\bar{x}^2)/(n-1)} \tag{7}$$

$$CV = 100 \times (s_{n-1}/\bar{x}) \tag{8}$$

Table 4.3. Tension Test Results

Sample	E	v	Tensile Strength	Yield Strength
#2	704 MPa	0.488	14.5 MPa	3.89 MPa
#3	658 MPa	0.491	14.7 MPa	2.83 MPa
#4	627 MPa	0.452	14.6 MPa	3.49 MPa
#6	710 MPa	0.458	15.0 MPa	4.26 MPa
#7	709 MPa	0.472	14.7 MPa	4.71 MPa
$\bar{x}$	**682 MPa**	**0.472**	**14.7 MPa**	**3.84 MPa**
S_{n-1}	37.1 MPa	0.017	0.213 MPa	0.720 MPa
CV	5.4 %	3.7%	1.4%	18.8%

4.1.2. Compression Test. Seven compression samples were tested using the procedure described in ASTM D6641 and modified in Section 3.2.2.2. The objective of this test was to determine the ultimate compressive strength for modeling purposes. As mentioned, the two points of validation were restricting failure within the testing fixture and preventing Euler Buckling. Results for bending at an approximate 2000 με are shown below in Table 4.4.

Table 4.4. Tension Percent Bending Results

	Strain 1 (Front)	Strain 2 (Back)	Percent Bending
Sample #1	1947.8 με	2004.7 με	1.4%
Sample #2	2063.3 με	2376.6 με	7.1%
Sample #3	2111.7 με	1106.8 με	31.2%
Sample #4	1999.9 με	1385.8 με	18.1%
Sample #5	2026.1 με	1971.0 με	1.4%
Sample #6	1980.9 με	1636.9 με	9.5%
Sample #7	1943.1 με	2213.9 με	6.5%

Failure strain of the material far exceeded the deformation capabilities of the strain gages and therefore percent bending at this value could not be determined. Regarding Table 4.4, Sample #3 and #4 exceeded a 10% strain bending value. According to ASTM D6641 Section 12.4.1, studies have shown that strain bending as much at 40% may have little to no effect on the compressive strength [34]. Because of this, if bucking occurred on only a portion of the specimens, but there was little to no variation of the compressive strength between these and the other samples, it could be assumed that the resulting strain bending had no significant influence. As shown in Table 4.5, the compressive strengths of each sample resulted in a low coefficient of variation. Therefore, it can be assumed that the bending did not affect the result and Sample #3 and #4 may be considered valid. It was

likely that the strain variations with samples #3 and #4 were caused by a failure of an individual strain gage. A compression sample was bisected after performing the test to show the interior effect of the compression on the triangular infill, shown in Figure 4.2.

Table 4.5. Compressive Strength of Oynx

	Compressive Strength
Sample #1	14.5 MPa
Sample #2	14.5 MPa
Sample #3	14.6 MPa
Sample #4	15.1 MPa
Sample #5	15.5 MPa
Sample #6	14.2 MPa
Sample #7	14.9 MPa
$\bar{x}$	**14.8 MPa**
S_{n-1}	0.43 MPa
CV	2.9%

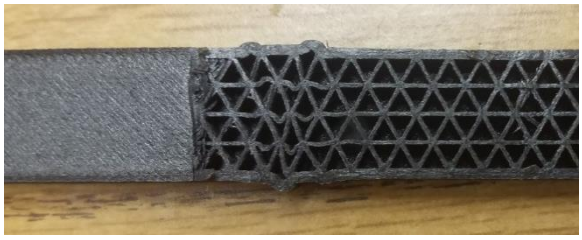

Figure 4.2. Bisected Compression Specimen

These compression strengths were determined using Equation 9. This equation was similar to Equation 4 used for the tension test. As mentioned, failure occurred outside of the capabilities of the strain gages so bending at failure could not be calculated. Average, standard deviation, and coefficient of variation were calculated using Equations 6-8 shown previously.

$$F^{cu} = P^{max}/A \tag{9}$$

4.1.3. Shear Test. ASTM D7078 was performed with adjustments mentioned in Section 3.2.2.3 to determine the shear modulus of Onyx for FEA purposes. Due to an apparent failure of a strain gage on Sample #1, Sample #2-#7 were used as the valid test specimens. Equation 10 was used to determine the shear chord modulus of elasticity. This equation was to be applied over a range of approximately 4000 με. For the value of shear stress and shear strain, Equations 11 and 12 were used respectively. Shear modulus results can be found in Table 4.6. Average, standard deviation, and coefficient of variation were again calculated using Equations 6-8 shown previously.

$$G^{chord} = \Delta\tau/\Delta\gamma \tag{10}$$

$$\tau_i = P_i/A \tag{11}$$

$$\gamma_i = |\varepsilon_{+45^\circ}| + |\varepsilon_{-45^\circ}| \tag{12}$$

Table 4.6. Shear Modulus of Elasticity of Onyx

Sample	G
#2	421 MPa
#3	452 MPa
#4	440 MPa
#5	426 MPa
#6	412 MPa
#7	418 MPa
$\bar{x}$	**428 MPa**
S_{n-1}	15.0 MPa
CV	3.5 %

4.2. BRIDGEBOT

4.2.1. Prototype. The design prototype, created to address the considerations described in Section 3.2.1 in order to perform as a mobile platform for bridge inspections, is shown below in Figure 4.3 with additional photos located in Appendix D. The drone,

being further referred to as the “BridgeBot”, utilized the benefits of both flying and traversing technologies through the development of a multimodal system. Using two methods of transportation allows the design to maneuver around obstacles and over overpasses while in traversing mode. Traversing also uses less battery power which will increase the duration of the bridge inspection that the drone can perform.

The proposed design took flight using four brushless DC outrunner motors, each providing approximately 67 N (15 lbs) of thrust. By simply switching the 47.0 cm (18.5-in) propellers for 54.6 cm (21.5 in), the system could be increased to nearly 98 N (22 lbs) of thrust. The objective was to maintain a minimum 2:1 ratio of thrust to drone weight for flight stability. Rotors were attached by four carbon fiber plate arms which were secured directly to the drone’s carbon fiber frame. Support walls were also added to these arms to increase rigidity during takeoff when forces were the greatest on the rotor arms.

Figure 4.3. BridgeBot Mobile Platform Prototype

Once in place beneath a bridge girder, two DC motors were used to engage the clamping system. With the help of beveled 3D printed Onyx gears, two lead screws on either side of the BridgeBot, as shown in Figure 4.4, drove the clamps horizontally to apply pressure against the edges of the flange above. Stationary columns ensured that the drone was at the proper offset distance from the girder for the system to grip the flange. By clamping on the edges, rather than above and below the beam, interaction with bolt heads and nuts, flange splice connection plates, or low hanging lateral bracing could be minimized or avoided completely. The clamps utilized a scissoring motion to maximize the range of flange sizes that a particular set of arms could engage. The proposed BridgeBot was applicable to a flange range of 38-47 cm (15-18.5 inches), but with a creation of various, interchangeable, custom carbon fiber arms, many other flange sizes could be achieved without modification to the frame of the drone. The clamping mechanism for the prototype was position controlled by linear potentiometers. This meant that a relation could be established between the potentiometer position and the location of the clamps. Flange sizes could then be related to a dial position on the remote controller or ground station to ensure that the grips were in the proper position for a particularly sized girder.

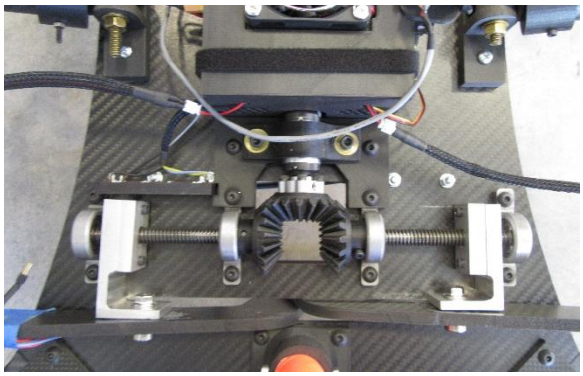

Figure 4.4. Beveled Gear Driven Clamping System

At the end of each clamping arm were the grips which also acted as the BridgeBot traversing mechanisms. These 3D printed Onyx wheels (Figure 4.5) were each powered by their own DC motor. The wheels were overlaid with a with a flexible urethane coating to increase the coefficient of friction against the beam to help with stability during inspection. In order to pass flange splice plate connections, the wheels required the ability to roll over a connection plate. The introduction of an inverted conical portion to the top of each wheel allowed the drone to ride up onto the connection plate while traversing along the bridge girder and keep the flange towards the center portion of the wheel.

Figure 4.5. 3D Printed Onyx Wheels

Speed and flight controllers, two 50V batteries, and landing gears were attached beneath the main carbon fiber structure of the drone. The landing gears, constructed of carbon fiber tubes, were attached using Onyx components to reduce weight and allow various custom connections. The landing gears also created a platform which supported the

easily interchangeable batteries so that flight duration could be increased quickly, without the need to recharge a permanently attached power source. These batteries were used to power the 50V flight controller, along with the 12V DC motors which drive the traversing and flying mechanisms. Other components on the drone that required a more rigid connection used aluminum 6061-T6. High stress components which must resist deformation were created using AISI 1045 steel. This included the wheel shaft and lead screw components. Approximate weights of major components are given in Table 4.7. The overall weight of the BridgeBot prototype was approximately 11.3 kg (25 lbs). Using 54.6 cm (21.5 in) propellers, a payload of approximately 9.1 kg (20 lbs) could be achieved while maintaining a 2:1 thrust ratio. Due to the major components being placed beneath the drone structure, inspection mechanisms could be placed above the platform, closest to the girder to which it is inspecting. Wireless cameras were also attached to arms on either side of the drone platform and above the central housing unit to show a potential inspection technique that the BridgeBot could perform. These cameras relayed real-time video to the control station to assist with positioning of the drone during flight tests.

Table 4.7. BridgeBot Component Approximate Weights

Component	Weight	
Unit	kg	lbs
Structure	2.3	5.0
Battery (2)	1.6	3.5
Rotors (4)	0.5	1.0
Central Housing	3.6	8.0
Flight Controller	0.5	1.0
Total	**11.3**	**25.0**

4.2.2. FEA Analysis of Structural System. In order to analyze the structural integrity of the drone and to view potential areas of concern, three loading simulations were performed within the Solidworks 2017 modeling software produced by Dassault Systèmes. This included loading during initial thrust, gravity loads while attached to the girder, and clamping forces produced by the traversing mechanism. Solidworks' default properties for Al 6061 – T6 and AISI 1045 steel were used in the model. Average carbon fiber properties discussed in Section 3.1.1 were used for a more generic simulation, rather than being company specific for the Clearwater Composite carbon fiber sheets used for the prototype. Onyx material properties determined during laboratory testing were designated where applicable within the model. These simulations were used to analyze the structural components of the drone and therefore all mechanical devices within the drone were removed. Figure 4.6a shows the Solidworks' model which was created while Figure 4.6b shows the reduced model used for simulation purposes. Component loads were then reintroduced as external loads. It is important to note that simulations were only used to evaluate the stress distribution throughout the structure. Exact values of stress were not a concern unless the approximate forces caused stresses which approached the limits of the material used within the area.

Quasi-static simulations within Solidworks produced the results found in the sections below. Solidworks software under these conditions assumed that the loads are applied slowly and gradually until reaching their full magnitude. Any inertial and damping forces were therefore neglected. A linear-elastic assumption was also made due to the linear response shown by the materials used within the study along with the goal of requiring all materials to stay within their elastic ranges. Using a curvature based, solid

mesh, with a maximum element size of 40 mm (1.57 in) and a minimum of 8 mm (0.31 mm), a mesh containing 54,668 elements and 106,789 nodes was achieved. This size mesh was chosen as a balance between precision of the final result and the computing power necessary to perform each simulation by reducing the element sizes until a sequential reduction produced a change in maximum stress of less than 3%.

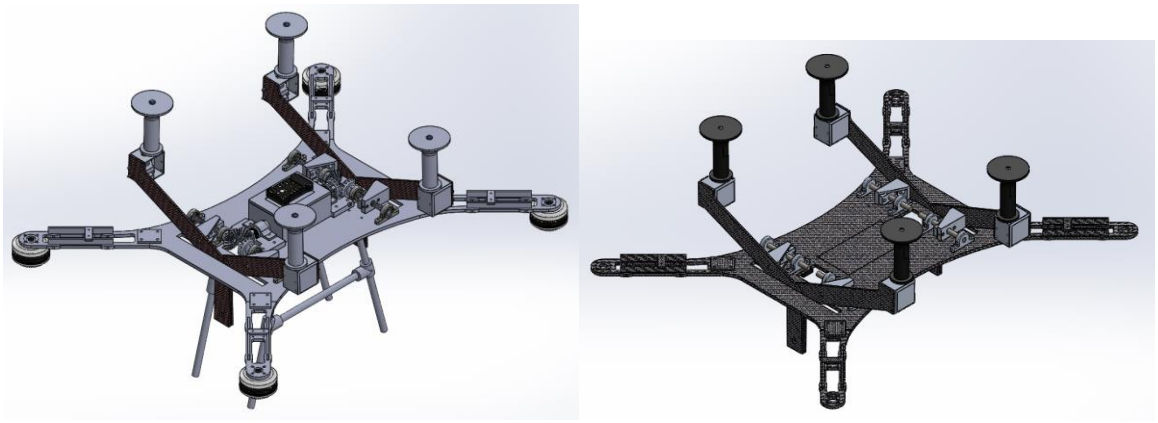

Figure 4.6. BridgeBot 3D Model:
Complete Model (left), Reduced Structural Model (right)

4.2.2.1. Initial thrust results. Loads applied for an initial thrust simulation are shown in Figure 4.7 along with the stress distribution results. For this model, loading gear connections beneath the drone were fixed to resist motion while 67 N (15 lbs) of uplift were applied in each rotor location. Other vertical loads shown include the central housing unit in blue, rotor dead loads in green, battery and flight controller loads in orange, and material self-weight in yellow. Stress results show that the location of maximum stress occurred in the assumed location at the cantilevered connection of the rotor arms to the main platform. The resultant stress was approximately 110 MPa (16 ksi) which was below

the yield strength of the carbon fiber in that location (1080 MPa (157 ksi)). The other areas of elevated stress that were apparent were due to bending forces at the slots cut for the clamping arms. Though the stresses found during the test were low compared to the yield strength, stress in these locations may lead to undesired deformations. With these results, rotor arms for a second prototype may require a design adjustment which carries the stresses across the body of the drone, past the slit for the clamping arms, in order to increase rigidity.

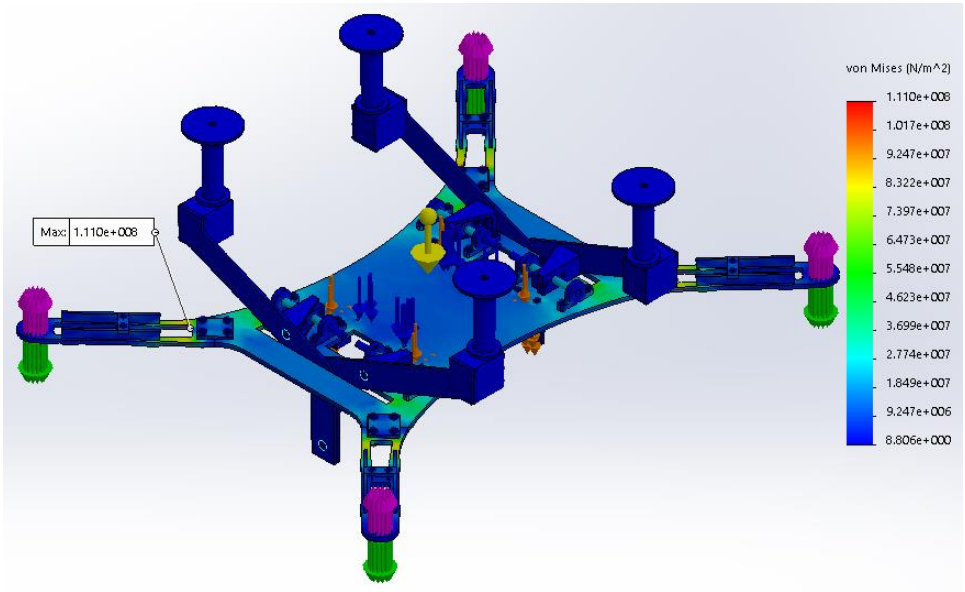

Figure 4.7. Initial Thrust Simulation

4.2.2.2. Gravity results. In order to determine the forces which were transferred though the BridgeBot design while traversing, the simulation was broken down into two individual simulations which could be superimposed for approximate total stress. Gravity simulations were performed which assumed a fixed connection between the wheels and the girder flanges. Thrust loads were removed since rotors would be off while the drone was

traversing along the girder. Results of this simulation are shown in Figure 4.8. Stresses were low and therefore not a concern for strengthening purposes. The simulation was instead used to help assure the validity of the model while other simulations were performed. The location of maximum stress occurred at the intersection of the 8 mm (0.31 in) steel shaft and the aluminum tube portion which houses the DC motors for traversing the structure.

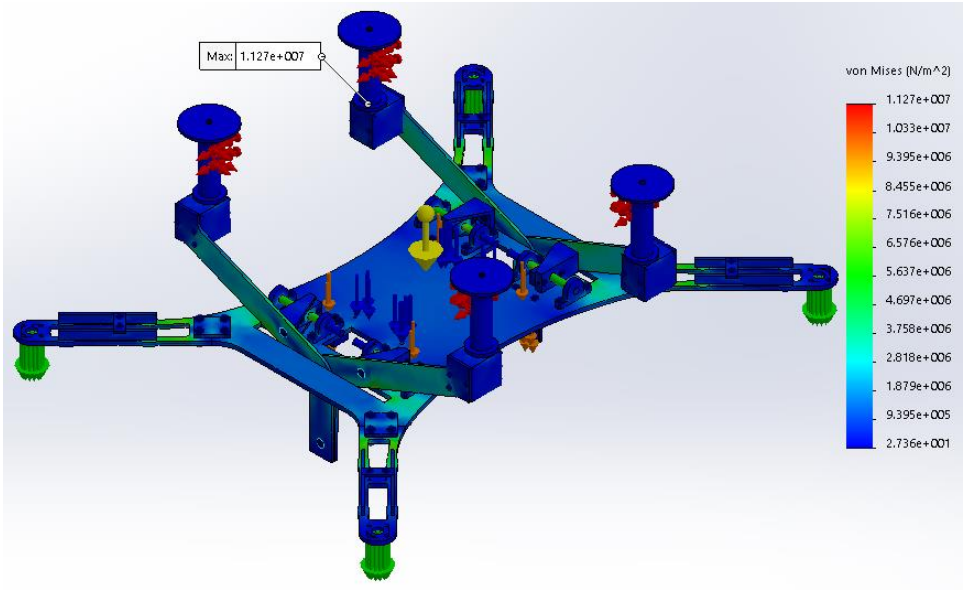

Figure 4.8. Gravity Simulation Results

4.2.2.3. Pure clamping results. For the pure clamping force simulation, standard gravity loads were applied, and the landing gear connections were fixed as in the case of the initial thrust simulation. An 89 N (20 lb) horizontal, outward force was placed on the wheels at the intersection of the bottom cylinder and the inverted conical top. This location was chosen due to it being the typical location where the wheel would be in contact with the bridge girder. Though the 89 N (20 lb) force was assumed for the simulation, the

magnitude was justified by the results discussed in Section 4.2.3. The stress distribution results shown in Figure 4.9 distinguish the same maximum stress location as the gravity simulation above. The summation of this stress with the result of the gravity test gave an approximate value of what the drone may experience while traversing a bridge girder. This estimated 126 MPa (18.3 ksi) value was below the 275 MPa (18.3 ksi) yield stress of Al 6061-T6 and therefore did not raise considerable concerns for a redesign, though increasing the thickness of the aluminum tube would reduce the stress.

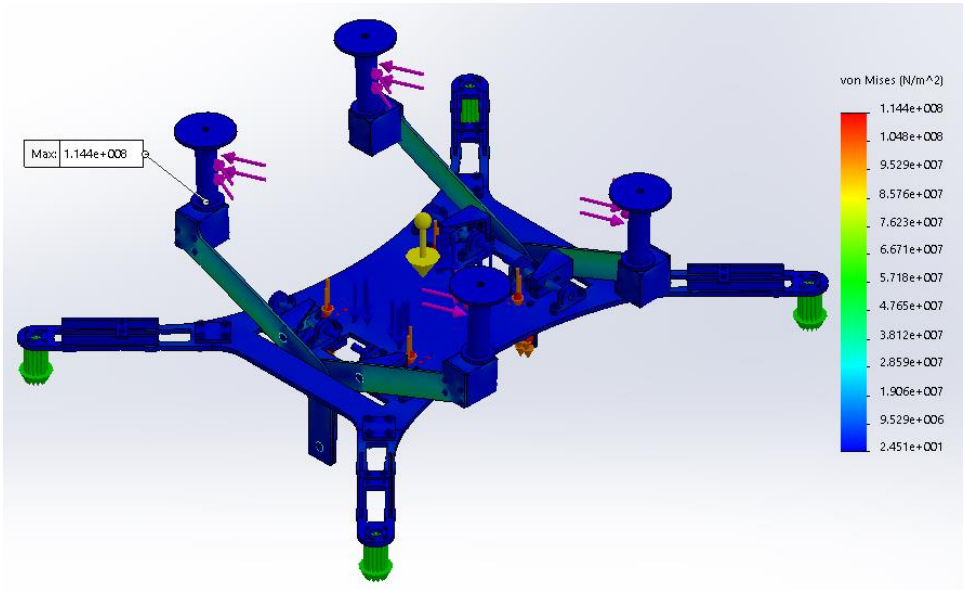

Figure 4.9. Clamping Simulation Results

4.2.3. Laboratory Testing. Two laboratory tests were performed to assess the drone prototype within the lab. These tests were performed to allow for a safe testing location where the drone could be closely inspected during the experimentation process for areas of concern.

4.2.3.1. Clamping strength test. The first official laboratory test was completed to determine the clamping strength of the BridgeBot. The result of this test was used to evaluate weak points within the BridgeBot traversing mechanism and to determine the appropriate force to be added into the FEA simulations described above. This test was performed prior to the figures in Section 4.2.1 and results of this test caused a slight adjustment to the prototype. The change is described below. A rigid frame was assembled as shown below so that the BridgeBot could be closely viewed from all angles (Figure 4.10). Both wheels of a clamping assembly were strapped individually to the rigid frame on either side. One of the straps included a 220 N (50 lb) dial hanging scale in order to measure the total force created by the clamping mechanism. Once attached to the rigid frame, the drone clamps were engaged, and clamping force was increased until the system reached a maximum value. This maximum load was classified as either one which damage occurred, or the system was showing very large deflections.

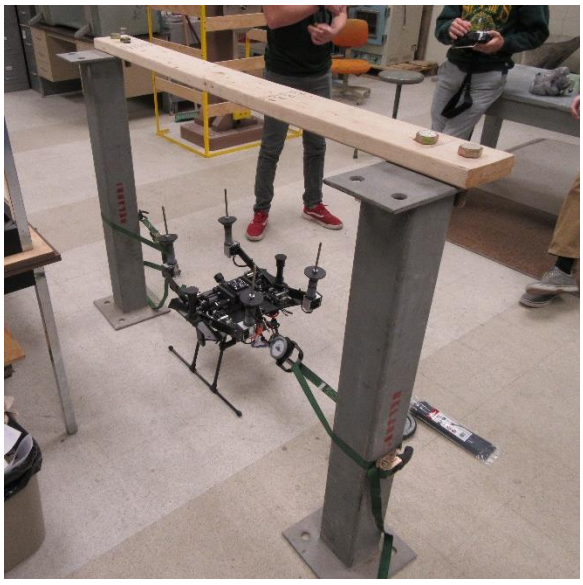

Figure 4.10. Rigid Frame Testing Assembly

For the first dataset, damage began to occur rather early in testing. Due to the force created by the lead screw on the traversing bracket, the Onyx portion began to delaminate (Figure 4.11). To confirm the results, the drone was rotated, and the test was performed on the second clamping mechanism. Crack initiation began at approximately 67-89 N (15-20 lbs), but it was chosen to continue the test due to the location of the damage. It was assumed that though delamination was occurring, the screws which attach the small Onyx bracket to the L-shaped aluminum bracket would limit the crack width as was seen at test completion. Testing was terminated at approximately 200 N (45 lbs) due to the large deflection of the wheel gearbox (Figure 4.12). It was decided that flipping the brackets would drive the Onyx material into compression and would be a simple solution for a second round of testing.

Figure 4.11. Delamination of Onyx Material at Lead Screw Bracket

For the second dataset, after flipping the lead screw connection bracket, the test was performed following the same procedure as previously mentioned. With this orientation, damage was not observed during testing and therefore it was decided to push the limit and

max out the dial gages which caused larger deflections than those in the first dataset. Though traversing tests across a beam flange and over obstacles had yet to be performed, it was assumed that 220 N (50 lbs) far exceeded the normal operating conditions of the drone. Strength of the mechanical system was deemed adequate, but deflections may need to be reevaluated once the necessary clamping force required for stable inspection operations is determined. After flipping the connection bracket, the horizontal motion of the wheels was restricted to approximately half of the original design. For future tests, rather than redesigning the body of the drone, it was decided that the small Onyx bracket would instead be formed out of Al 6061-T6 and the lead screw traversing bracket would remain in its original orientation (Figure 4.13). Using aluminum would remove the delamination concern while providing the necessary strength. This change is shown in Section 4.2.1.

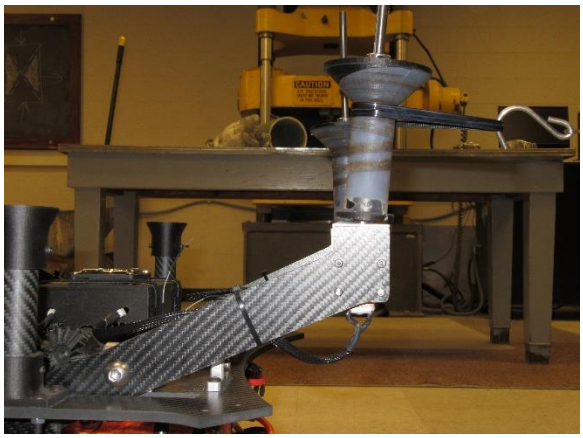

Figure 4.12. Visible Deflection of Wheel Gearbox

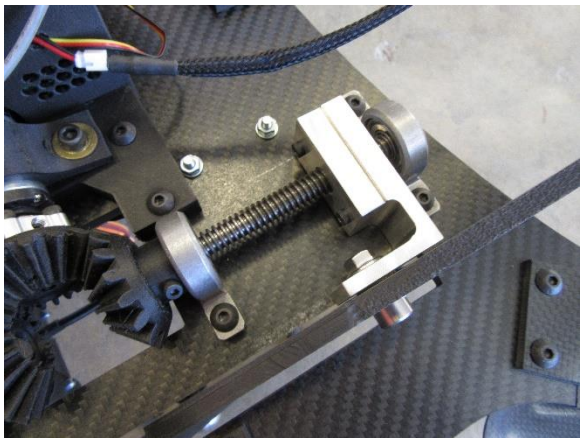

Figure 4.13. Aluminum Lead Screw Traversing Bracket

4.2.3.1. Complete system laboratory test. A complete system test was performed to validate the BridgeBot prototype. This test evaluated all current systems; flying, clamping, and traversing. The setup below in Figure 4.14 was constructed of wood to evaluate the drone at a low elevation for close eye inspection. Using plywood, a 43.2 cm (17 in) plank was formed to simulate the bottom flange of a steel girder. The BridgeBot launched from ground level upwards until it reached the wood plank. Once beneath the test fixture, stabilized by the standoff columns between each set of wheels, the clamping system was successfully engaged towards the base of each wheel. After traversing a short distance, the drone then settled at the base of the inverted conical section (Figure 4.15). The traversing mechanism was tested back and forth along the wooden flange for several passes until the team was comfortable with the results. Rotors were then throttled upwards as the clamping mechanism was slowly disengaged. A loose connection caused issued while disengaging from the test setup, but this was easily corrected. Once the clamps spread past the extent of the plywood, the throttle was lowered until the drone landed back on the ground. While landing and turning off the rotors, the flexibility of the arms seen during

FEA simulations at the cantilevered connection of the rotor arms caused the propellers to reflex and hit the wires attached to the underside of the arms. This forcefully dislodged the wire connection, but no damage to the wires or the frame occurred.

Several conclusions were made from the results of the complete system test. Concerns mentioned in Section 4.2.2.1 regarding the rotor arms were apparent during the initial takeoff, while rotors were throttled against the base of the test fixture, and during landing. Undesired flexing occurred at the cantilevered connection of the rotor arm to the main frame and at the ends of the slits in the frame which was cut for the clamping mechanisms. This did not hinder the flight capabilities, but it did cause a slight bouncing motion to occur during takeoff and cause the wires to disconnect as mentioned above. Though clamping force was not analyzed while traversing the setup, large deflection of the wheels was not seen compared to the clamping test at high loads. Therefore, it could be assumed that the clamping mechanism can provide more than the minimum force necessary to clamp onto a girder and perform an inspection. Using a position-controlled clamping mechanism without yet establishing a relation between flange sizes and a position on the remote controller did not cause an issue during the test but being within a close distance to the lab setup made this a possibility. On full size structures, this would not be an option. If the size of the girder is unknown, a position-controlled sensor would also not be as efficient.

Figure 4.14. Complete System Test Laboratory Setup

Figure 4.15. Fully Engaged Clamping System

5. CONCLUSIONS AND RECOMMENDATIONS

5.1. CONCLUSIONS

The objective of this research was to design a mobile platform that may be mounted with cameras and sensors to complete a thorough bridge inspection. Through material testing, FEA simulations, and laboratory testing, a BridgeBot prototype was designed for use on steel girder bridge systems. The drone, with an overall weight of approximately 11.3 kg (25 lbs) was able to remain below the FAA limitation of 24.9 kg (55 lbs) while being able to carry a payload of 9.1 kg (20 lbs). This payload should allow for numerous inspection attachments to be implemented. During laboratory testing, the BridgeBot performed each mode of transportation with minimal issues. The flying system was able to safely takeoff and fly beneath the laboratory setup with enough stability to engage the clamping mechanism. Once beneath the girder, the drone was able to fully clamp onto the wooded test setup and traverse in each direction. Disengaging the clamps and returning to the ground safely had a few issues due to a loose connection and large deformations of the rotor arms but a design update could fix these concerns for future testing. Having the ability to transition quickly and effectively between modes of transportation allows the drone to avoid obstacles and transfer between bridge girders without the assistance of inspectors. Future work will confirm the validity of the design to safely and efficiently be used to perform a bridge inspection, but the initial prototype showed promising results. The research team believed the prototype was a valid initial design that can be modified into a practical mobile platform for bridge inspections that will increase inspector safety while decreasing time, cost, risk, and traffic control.

5.2. RECOMMENDATIONS FOR FUTURE WORK

Future work can be directed to finalize the design and build an improved prototype. Although the BridgeBot version 1 initially proved to have many of the necessary capabilities for an efficient mobile platform for bridge inspections, the following recommendations were made for the creation of BridgeBot version 2.

- An automatic girder detection system will likely need to be installed to simplify the clamp engagement process. Current manual systems rely completely on the ability and control of the pilot. An automated system would reduce the experience level needed for drone positioning.
- The clamping mechanisms on BridgeBot version 1 are position controlled. A pressure or strain-controlled system could assist in its automation process so that the necessary force is applied to engage the system and keep the drone stable through flange size transitions.
- A redesign for a more rigid rotor arm is necessary for stable flight and a safe takeoff and landing to occur. This design will likely need to distribute loads farther into the main frame of the drone, past the slits cut for the clamping mechanism.
- The current prototype does not have location tracking. GPS has proven to lose connection beneath the deck with drones discussed in Section 2.3.2 therefore some other means of position control will likely be necessary.
- Additional laboratory tests on the performance of the traversing mechanism are needed. This should include foreseen obstacles like flange splice connections, variable girder widths and depths, girder impact damage, etc.

Once a second prototype is constructed, or if it is chosen to proceed with BridgeBot version 1, it is recommended to proceed with full scale testing. This testing is expected to be completed with a DOT bridge inspector present to clarify questions and describe possible inspection scenarios. These tests would also quantify drone battery life and help provide the basics for a cost comparison with traditional inspection techniques. Once a platform has been finalized, after performing well through dynamic load situations at the maximum payload, potential inspection attachments can be researched and implemented.

APPENDIX A.

SUMMARY OF SMALL UNMANNED AIRCRAFT RULE (PART 107) [13]

FAA News

Federal Aviation Administration, Washington, DC 20591

June 21, 2016

SUMMARY OF SMALL UNMANNED AIRCRAFT RULE (PART 107)

Operational Limitations	• Unmanned aircraft must weigh less than 55 lbs. (25 kg). • Visual line-of-sight (VLOS) only; the unmanned aircraft must remain within VLOS of the remote pilot in command and the person manipulating the flight controls of the small UAS. Alternatively, the unmanned aircraft must remain within VLOS of the visual observer. • At all times the small unmanned aircraft must remain close enough to the remote pilot in command and the person manipulating the flight controls of the small UAS for those people to be capable of seeing the aircraft with vision unaided by any device other than corrective lenses. • Small unmanned aircraft may not operate over any persons not directly participating in the operation, not under a covered structure, and not inside a covered stationary vehicle. • Daylight-only operations, or civil twilight (30 minutes before official sunrise to 30 minutes after official sunset, local time) with appropriate anti-collision lighting. • Must yield right of way to other aircraft. • May use visual observer (VO) but not required. • First-person view camera cannot satisfy "see-and-avoid" requirement but can be used as long as requirement is satisfied in other ways. • Maximum groundspeed of 100 mph (87 knots). • Maximum altitude of 400 feet above ground level (AGL) or, if higher than 400 feet AGL, remain within 400 feet of a structure. • Minimum weather visibility of 3 miles from control station. • Operations in Class B, C, D and E airspace are allowed with the required ATC permission. • Operations in Class G airspace are allowed without ATC permission. • No person may act as a remote pilot in command or VO for more than one unmanned aircraft operation at one time. • No operations from a moving aircraft. • No operations from a moving vehicle unless the operation is over a sparsely populated area. • No careless or reckless operations. • No carriage of hazardous materials.

	• Requires preflight inspection by the remote pilot in command. • A person may not operate a small unmanned aircraft if he or she knows or has reason to know of any physical or mental condition that would interfere with the safe operation of a small UAS. • Foreign-registered small unmanned aircraft are allowed to operate under part 107 if they satisfy the requirements of part 375. • External load operations are allowed if the object being carried by the unmanned aircraft is securely attached and does not adversely affect the flight characteristics or controllability of the aircraft. • Transportation of property for compensation or hire allowed provided that- o The aircraft, including its attached systems, payload and cargo weigh less than 55 pounds total; o The flight is conducted within visual line of sight and not from a moving vehicle or aircraft; and o The flight occurs wholly within the bounds of a State and does not involve transport between (1) Hawaii and another place in Hawaii through airspace outside Hawaii; (2) the District of Columbia and another place in the District of Columbia; or (3) a territory or possession of the United States and another place in the same territory or possession. • Most of the restrictions discussed above are waivable if the applicant demonstrates that his or her operation can safely be conducted under the terms of a certificate of waiver.
Remote Pilot in Command Certification and Responsibilities	• Establishes a remote pilot in command position. • A person operating a small UAS must either hold a remote pilot airman certificate with a small UAS rating or be under the direct supervision of a person who does hold a remote pilot certificate (remote pilot in command). • To qualify for a remote pilot certificate, a person must: o Demonstrate aeronautical knowledge by either: ▪ Passing an initial aeronautical knowledge test at an FAA-approved knowledge testing center; or ▪ Hold a part 61 pilot certificate other than student pilot, complete a flight review within the previous 24 months, and complete a small UAS online training course provided by the FAA. o Be vetted by the Transportation Security Administration. o Be at least 16 years old. • Part 61 pilot certificate holders may obtain a temporary remote pilot certificate immediately upon submission of their application for a permanent certificate. Other applicants will obtain a temporary remote pilot certificate upon successful completion of TSA security vetting. The FAA anticipates that it will be able to issue a temporary remote pilot certificate within 10 business days after receiving a completed remote pilot certificate application. • Until international standards are developed, foreign-

	certificated UAS pilots will be required to obtain an FAA-issued remote pilot certificate with a small UAS rating. A remote pilot in command must: • Make available to the FAA, upon request, the small UAS for inspection or testing, and any associated documents/records required to be kept under the rule. • Report to the FAA within 10 days of any operation that results in at least serious injury, loss of consciousness, or property damage of at least $500. • Conduct a preflight inspection, to include specific aircraft and control station systems checks, to ensure the small UAS is in a condition for safe operation. • Ensure that the small unmanned aircraft complies with the existing registration requirements specified in § 91.203(a)(2). A remote pilot in command may deviate from the requirements of this rule in response to an in-flight emergency.
Aircraft Requirements	• FAA airworthiness certification is not required. However, the remote pilot in command must conduct a preflight check of the small UAS to ensure that it is in a condition for safe operation.
Model Aircraft	• Part 107 does not apply to model aircraft that satisfy all of the criteria specified in section 336 of Public Law 112-95. • The rule codifies the FAA's enforcement authority in part 101 by prohibiting model aircraft operators from endangering the safety of the NAS.

APPENDIX B.

POTENTIAL AID PROVIDED BY UAVs [25]

REPORT REQUIREMENT	AIDED BY UAS? (Y/N)	HOW IT CAN BE AIDED OR WHY IT CANNOT
Identification	N	This information will be known prior to any field inspection with a UAS.
Structure Type and Material	Y	High Resolution photos of the structure can display the type and the material of the bridge.
Age and Service	Y	The age of the bridge can only be estimated from imagery collected by a UAS; however, the surrounding area can be recorded by a UAS
Geometric Data	Y	Previous records of geometric values can be compared with geometries acquired from 3D reconstructions of the imagery collected during a UAS inspection
Navigation Data	Y	Many forms of pier protection could be identified and waterway clearances can be measured from point clouds generated from 3D reconstructions of UAS imagery.
Classification	N	This information should be known prior to any field inspection. UAS flights are not needed for determining the facility that is using the bridge.
Load Rating and Posting	N	This would be better performed by the engineer on the ground. Signage is easily accessible from the ground.
Proposed Improvements	N	This is a section written up by the engineer on how to improve the bridge condition. However, the imagery provided could aid the engineer in accessing the bridge.
Inspections	N	This section refers to previous inspections performed. This data would be recorded previously.

REPORT REQUIREMENT	AIDED BY UAS? (Y/N)	HOW IT CAN BE AIDED OR WHY IT CANNOT
Deck	Y	Geometry of Deck as well as presence of defects could be identified via high resolution imagery
Superstructure	Y	Presence of cracks and other defects can be identified as well as monitored though imagery collected from regular UAS flights over time
Substructure	Y	Presence of cracks and other defects can be identified as well as monitored though imagery collected from regular UAS flights
Channel and Channel Protection	Y	Hydraulic countermeasures could be visually monitored by regular inspection by a UAS. The bank conditions can be monitored through low altitude flights.
Culvert	Y	Any exterior blockage of culverts that are not entirely submerged can be identified by a UAS

REPORT REQUIREMENT	AIDED BY UAS? (Y/N)	HOW IT CAN BE AIDED OR WHY IT CANNOT
Structural Evaluation	Y	Presence of cracks and other defects can be visually identified as well as monitored though imagery collected from regular UAS flights
Deck Geometry	Y	The geometry of the deck can be recorded in imagery with proper ground control
Under-Clearances	Y	Clearance values and opening can be potentially measured by 3D reconstructions of the UAS imagery
Waterway Adequacy	Y	Waterway openings can be recording and captured with high resolution photography from a UAS
Approach Roadway Alignment	Y	The alignment of the bridge roadway access can be recreated via low altitude flights; orthophotos can be generated from reconstructions of the UAS imagery
Traffic Safety Features	Y	A UAS can provide views of the outer side of bridge railings
Scour Critical Bridges	Y/N	As probing is not currently possible with a typical UAS, testing for scour is not possible; however, bank monitoring from regular inspection is possible with aerial imagery

APPENDIX C.

ONYX MATERIAL DATASHEET [31]

Markforged

Same Day. Strong Parts.

Designed to strong, high quality, uncompromised parts, Markforged 3D Printers™ are the world's first 3D printers capable of printing continuous carbon fiber, Kevlar®, and fiberglass. Using a patent pending Continuous Filament Fabrication (CFF™) print head alongside a Fused Filament Fabrication (FFF) print head, Markforged printers can create functional parts by combining our specially tuned nylon with continuous fiber filaments.

3D Print Parts:

- With a higher strength-to-weight ratio than 6061-T6 Aluminum
- Up to 27x stiffer than ABS
- Up to 24x stronger than ABS

Mechanical Properties of Continuous Fibers

Property	Test Standard	Carbon CFF	Kevlar® CFF	Fiberglass CFF	HSHT Glass CFF
Tensile Strength (MPa)	ASTM D3039	700	610	590	600
Tensile Modulus (GPa)	ASTM D3039	54	27	21	21
Tensile Strain at Break (%)	ASTM D3039	1.5	2.7	3.8	3.9
Flexural Strength (MPa)	ASTM D790*	470	190	210	420
Flexural Modulus (GPa)	ASTM D790*	51	26	22	21
Flexural Strain at Break (%)	ASTM D790*	1.2	2.1	1.1	2.2
Compressive Strength (MPa)	ASTM D6641	320	97	140	192
Compressive Modulus (GPa)	ASTM D6641	54	28	21	21
Compressive Strain at Break (%)	ASTM D6641	0.7	1.5	n/a	n/a
Heat Deflection Temperature (°C)	ASTM D648 Method B	105	105	105	150
Density (g/cm^3)	N/A	1.4	1.25	1.6	1.6
Izod Impact — notched (J/m)	ASTM D256-10 Method A	958	1873**	2603	3117

*Measured by a method similar to ASTM D790
**Two samples measured instead of 5

Dimensions and Construction of Fiber Composite Test Specimens

- Test plaques used in this data are fiber reinforced unidirectionally (0° Plies)
- Tensile test specimens: 9.8 in (L) x 0.5 in (H) x 0.048 in (W) (CF composites), 9.8 in (L) x 0.5 in (H) x 0.08 in (W) (GF and aramid composites)
- Compressive test specimens: 5.5 in (L) x 0.5 in (H) x 0.085 in (W) (CF composites), 5.5 in (L) x 0.5 in (H) x 0.12 in (W) (aramid and GF composites)
- Flexural test specimens: 3-pt. Bending, 4.5 in (L) x 0.4 in (W) x 0.12 in (H)
- Heat-deflection temperature at 0.45 MPa, 66 psi (ASTM D648-07 Method B)

Tensile, Compressive, Strain at Break, and Heat Deflection Temperature data were provided by an accredited 3rd party test facility. Flexural data was prepared by Markforged, Inc. The above specifications were met or exceeded.

With the exception of the Onyx One, Markforged Industrial Strength 3D Printers are capable of printing a wide variety of fiber reinforcement patterns creating both anisotropic and quasi-isotropic ply constructions. This data sheet gives reference and comparison material properties using one possible set of standards-compliant ASTM plaques printed with a production Markforged 3D printer.

However, part and material performance will vary by ply design, part design, end-use conditions, test conditions, build conditions, and the like.

Mechanical Properties of Nylon

Property	Test Standard	Tough Nylon	Onyx
Tensile Modulus (GPa)	ASTM D638	0.94	1.4
Tensile Stress at Yield (MPa)	ASTM D638	31	36
Tensile Strain at Yield (%)	ASTM D638	27	25
Tensile Stress at Break (MPa)	ASTM D638	54	30
Tensile Strain at Break (%)	ASTM D638	260	58
Flexural Strength (MPa)	ASTM D790*	32	81
Flexural Modulus (GPa)	ASTM D790*	0.84	2.9
Flexural Strain at Break (%)	ASTM D790*	n/a	n/a
Heat Deflection Temperature (°C)	ASTM D648 Method B	49 140†	145
Density (g/cm^3)	N/A	1.10	1.18
Izod Impact — notched (J/m)	ASTM D256-10 Method A	1015	334

*Measured by a method similar to ASTM D790
†Heat deflection temperature of a beam with less than 10% HSHT Glass added, see below for details

Dimensions and Construction of Plastic Test Specimens

- Tensile test specimens: ASTM D638 type IV beams
- Flexural test specimens: 3-pt. Bending, 4.5 in (L) x 0.4 in (W) x 0.12 in (H)
- Heat-deflection temperature at 0.45 MPa, 66 psi (ASTM D648-07 Method B)
- Flexural Strain at Break is not available because nylon does not break before the test ends

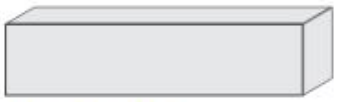

127 layer Nylon FFF Beam:
(not to scale)
Heat Deflection: 49 °C

Design Principles for Bending

Markforged CFF™ technology **reinforces** 3D plastic parts with 10x stronger and 20x stiffer continuous fibers.

The above Material Properties therefore are **combined** in a part automatically by our Eiger software (although users may also customized the fiber distribution per layer).

In automatic mode, Markforged's Eiger software defaults to creating embedded Sandwich Panels — well-known reinforced structures widely used in aerospace and construction that provide excellent **bending** performance.

Overall part stiffness and strength, represented by tensile and compressive Material Properties above, depends very much upon fiber content, and is strongly related to the amount of fiber the user chooses for a part.

However, per engineering sandwich theory, **flexural** or bending performance tends to benefit **strongly** from **modest** reinforcement in a sandwich panel form (see images on the right).

For more information, please our more detailed "Thermomechanical Stability" white paper.

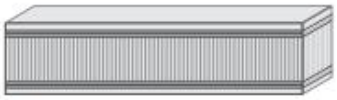

127 layer HSHT Sandwich Beam:
(not to scale)
117 layers nylon,
10 layers HSHT Glass CFF (~10% by vol.)
Heat Deflection: 140 °C

127 layer HSHT Filled Beam:
(not to scale)
2 layers Nylon,
125 layers HSHT Glass CFF:
Heat Deflection: 150 °C

markforged.com printstronger@markforged.com +1 617.666.1935

APPENDIX D.

ADDITIONAL BRIDGEBOT PROTOTYPE PHOTOS

BIBLIOGRAPHY

[1] American Society of Civil Engineers, "Infrastructure Report Card - Bridges," ASCE, 2017.

[2] T. W. Ryan, E. J. Mann, Z. M. Chill and B. T. Ott, "Bridge Inspector's Reference Manual (BIRM)," Federal Highway Administration, 2012.

[3] Federal Highway Administration, "Bridge Management," U.S. Department of Transportation, [Online]. Available: https://www.fhwa.dot.gov/bridge/management/.

[4] Federal Highway Administration, "23 CFR part 650 subpart C- National Bridge Inspection Standards," U.S. Department of Transportation, 2004.

[5] A. Link, "'Snooper truck' inspects bridges," Post-Bulletin Company, LLC, 05 April 2016. [Online]. Available: https://www.postbulletin.com/news/local/snooper-truck-inspects-bridges/article_89e240be-12bb-5a74-9ffe-d86e98cfe04f.html.

[6] Northeast Work & Safety Boats, "Barges with Man Lift," 2018. [Online]. Available: http://www.safetyboats.com/services-equipment/barges-with-man-lift.

[7] Canadian Rope Access Specialists Inc, "Municipal Bridge Inspections," 2013. [Online]. Available: http://www.cras.ca/portfolio/municipal-bridge-inspections/.

[8] Federal Highway Administration, "Facts and Statistics - Work Zone Safety," U.S. Department of Transportation, 2017. [Online]. Available: https://ops.fhwa.dot.gov/wz/resources/facts_stats/safety.htm.

[9] R. Salit, "Bucket trucks back in use following Sakonnet River Bridge incident," The Providence Journal, 2016. [Online]. Available: http://waltham.wickedlocal.com/news/20160912/bucket-trucks-back-in-use-following-sakonnet-river-bridge-incident?start=2.

[10] Federal Highway Administration, "2017 NBI ASCII Data," U.S. Department of Transportation, 2017.

[11] Federal Highway Administration, "Recording and Coding Guide for the Structure Inventory and Appraisal of the Nation's Bridges: Report No. FHWA-PD-96-001," U.S. Department of Transportation, 1995.

[12] Federal Aviation Administration, "Fact Sheet - Unmanned Aircraft Systems (UAS)," U.S. Department of Transportation, 2015. [Online]. Available: https://www.faa.gov/news/fact_sheets/news_story.cfm?newsId=18297.

[13] Federal Aviation Administration, "Summary of Small Unmanned Aircraft Rule (Part 107)," U.S. Department of Transportation, 2016.

[14] Federal Aircraft Administration, "14 CFR part 107 - Small Unmanned Aircraft Systems," U.S. Department of Transportation, 2016.

[15] A. Mazumdar, "Mag Feet: A Robotic Device for the Inspection of Steel Bridge Structures," Massachusetts Institue of Technology, 2009.

[16] H. M. La, T. H. Dinh, N. H. Pham, Q. P. Ha and A. Q. Pham, "Automated Robotic Monitoring and Inspection of Steel Structures and Bridges," 2017. arXiv:1705.04888v1 [cs.RO]

[17] N. H. Pham, H. M. La, Q. P. Ha, Q. P. Dang, V. H. Anh and Q. H. Dinh, "Visual and 3D Mapping for Steel Bridge Inspection Using a Climbing Robot," in *33rd International Symposium on Automation and Robotics in Construciton (ISARC 2016)*, 2016.

[18] T. S. Naguyen and M. H. La, "Development of a Steel Bridge Climbing Robot," University of Nevada, Reno, 2018. arXiv:1803.08209v2 [cs.RO]

[19] S. Chase and M. Edwards, "Developing a Tele-Robotic Platform for Bridge Inspection," University of Virginia, 2011.

[20] N. Hallermann and G. Morganthal, "Visual inspection strategies for large bridges using Unmanned Aerial Vehicles (UAV)," Bauhaus-Universitat Weimar, Weimar, Germany, 2014.

[21] J. Zink and B. LoveLace, "Unmanned Aerial Vehicle Bridge Inspection Demonstration Project," Office of Bridges & Structures, Collins Engineers, Inc., 2015.

[22] J. A. Bridge, P. G. Ifju, T. J. Whitley and A. P. Tomiczek, "Use of Small Unmanned Aerial Vehicles (sUAV) for Structural Inspection," University of Florida, 2018.

[23] G. Morgenthal and N. Hallermann, "Quality Assessment of Unmanned Aerial Vehicle (UAV) Based Visual Inspection of Structures. Reprinted from Advances in Structural Engineering," Multi-Science Publishing Co. LTD., 2014.

[24] B. Chan, H. Guan, J. Jo and M. Blumenstein, "Towards UAV-based bridge inspection systems: a review and an application perspective," *Structural Monitoring and Maintenance,* vol. 2, no. 3, pp. 280-300, 2015.

[25] D. T. Gillins, C. E. Parrish and M. N. Gillins, "Cost-Effective Bridge Safety Inspections Using Unmanned Aerial Vehicles (UAVs)," Pacific Northwest Transportation Consortium (PacTrans), 2016.

[26] T. Dorsey, "State DOTs Using Drones to Improve Safety, Collect Data and Cut Costs," American Association of State Highway and Transportation Officials, 2016.

[27] Clearwater Composites, "Properties of Carbon Fiber," Clearwater Composites, LLC, 2018. [Online]. Available: https://www.clearwatercomposites.com/resources/properties-of-carbon-fiber/.

[28] MatWeb, "Overview of materials for Epoxy/Carbon Fiber Composite," MatWeb, LLC, [Online]. Available: http://www.matweb.com/search/datasheet.aspx?matguid=39e40851fc164b6c9bda29d798bf3726&ckck=1.

[29] Clearwater Composites, "1/4" Carbon Fiber Plate," Clearwater Composites, LLC, [Online]. Available: https://www.clearwatercomposites.com/product/1-4-carbon-fiber-plate/.

[30] A. Crease, "Introducting Our New Markforged Material: Onyx," Markforged, 2016. [Online]. Available: https://markforged.com/blog/introducing-our-new-markforged-material-onyx/.

[31] Markforged, "Material Data Sheet," Markforged, 2016.

[32] Federal Highway Administration, "Post-1945 Highway Bridge Engineering," U.S. Department of Transportation, [Online]. Available: https://www.environment.fhwa.dot.gov/env_topics/historic_pres/post1945_engineering/this_bridge.aspx.

[33] American Society for Testing and Materials, "D3039/D3039M-14 Standard Test Method for Tensile Properties of Polymer Matrix Composite Materials," ASTM International, 2014.

[34] American Society for Testing and Materials, "D6641/D6641M-16 Standard Test Method for Compressive Properties of Polymer Matrix Composite Materials Using a Combined Loading Compression (CLC) Test Fixture," ASTM International, 2016.

[35] American Society for Testing and Materials, "D7078/D7078-12 Standard Test Method for Shear Properties of Composite Materials by V-Notched Rail Shear Method," ASTM International, 2012.

[36] P. H. Mott and C. M. Roland, "Limits to Poisson's ratio in isotropic materials - general result for arbitrary deformation," Chemistry Division, Naval Research Laboratory, 2010.

VITA

Clayton A. Fritsche was born in Perryville, Missouri and raised in the small town of Frohna, Missouri. At a young age, Clayton could frequently be found disassembling and reforming remote-controlled vehicles, woodworking, or assisting his father with construction projects. His passion grew and evolved into a love for design. He was later introduced to Structural Engineering at Missouri University of Science and Technology.

In 2013, Clayton began his Civil Engineering bachelor's degree which he later completed with a 4.0 cumulative G.P.A. in 2017. During his undergraduate education, Clayton was a member of Beta Sigma Psi fraternity, Chi Epsilon honor society, the Steel Bridge design team, and the American Society of Civil Engineers. Internships throughout his years at Missouri S&T helped Clayton gain valuable real-world experience before continuing into graduate school in August of 2017.

In the pursuance of Clayton's master's degree, he participated in additional internships where he discovered his passion for historical renovation and repair. He also continued his work with the Steel Bridge design team, became Vice-President and later President of Chi Epsilon, and became a graduate teaching assistant for the undergraduate material testing lab where he had the pleasure of teaching over 120 students. Clayton Fritsche received his Master of Science degree in Civil Engineering in May of 2019 from the Missouri University of Science and Technology. He chose to begin his professional career performing structural consulting in St. Louis, Missouri, forever grateful for those at Missouri S&T.